Direct simulation of drying colloidal suspension on substrate using immersed free surface model

Masahiro Fujita [a],*, Osamu Koike [b], Yukio Yamaguchi [b]

[a] *Department of Mathematics, Josai University, Tokyo 102-0093, Japan*
[b] *Department of Chemical System Engineering, The University of Tokyo, Tokyo 113-8656, Japan*

A B S T R A C T

This paper presents a new direct simulation method for a drying colloidal suspension on a substrate. A key issue of the present method is the immersed free surface model proposed by the authors, which enables us to estimate accurately and efficiently capillary forces exerted on particles on a free surface. Using the immersed free surface model along with immersed boundary method and level set method, the present method leads to a three-way coupling of the fluid flow, the free surface motion and the particle motion. In addition, the present method includes a way of curvature estimation using virtual grid differencing to calculate accurately a surface tension. The way of curvature estimation is quantitatively validated through the simulation of a still droplet. The immersed free surface model is quantitatively validated through the simulation of a sphere moving across a free surface and the simulation of two spheres moving along a free surface. Finally, simulations of drying colloidal suspension containing 130 particles are performed to demonstrate the applicability of the present method to actual systems.

© 2014 The Authors. Published by Elsevier Inc. This is an open access article under the CC BY-NC-ND license (http://creativecommons.org/licenses/by-nc-nd/3.0/).

1. Introduction

Drying of colloidal suspension on a substrate is a key process to fabricate particulate films that constitute various electronic devices, such as solar cells, flat panel displays and biological/chemical sensors [1]. The colloidal particles in a suspension spontaneously form a variety of microstructures on the substrate during drying [2–8]. The microstructure formation of the colloidal particles is a type of self-organization. Elucidation of the self-organization is crucial to control the microstructures of the colloidal particles. During drying, the colloidal particles are influenced by various non-linear interactions, such as contact interaction, van der Waals interaction, electrostatic interaction, capillary interaction and hydrodynamic interaction including thermal fluctuation of a solvent. A simulation of drying colloidal suspension is a major challenge even though computational fluid dynamics is now well developed. Recently, many researchers have been performed macroscopic simulations of the drying colloidal suspension [9–13], in which the evolution of the solid phase fraction in the suspension has been solved. Although the macroscopic simulations are applicable to systems in actual size, the microstructures of the colloidal particles cannot be obtained. On the other hand, several researchers have addressed direct simulations of the drying colloidal suspension [14,15], in which the motion of each particle has been solved. Although the direct simulation is rather expensive in computation than the macroscopic simulation, it has the advantage of obtaining the microstructures of the colloidal particles during drying.

---

* Corresponding author.
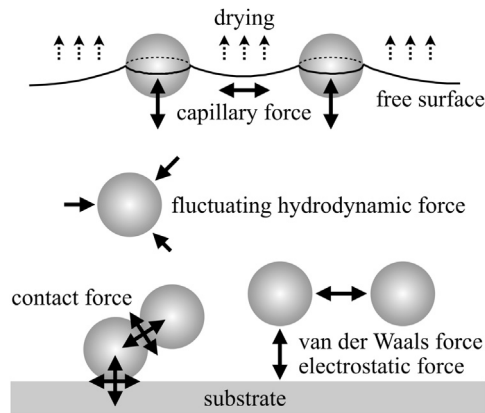 *E-mail address:* fujita@josai.ac.jp (M. Fujita).

Fig. 1. Forces exerted on colloidal particles that are included in the present simulation method.

For the direct simulation of the drying colloidal suspension, mesoscale gas–liquid–solid three phase flow with phase change should be taken into consideration. The problem can be divided into two issues; mesoscale solid–fluid two phase flow and gas–liquid two phase flow with phase change. Firstly, there are two issues in the mesoscale solid–fluid two phase flow. They are to apply the no-slip boundary condition on the solid–fluid interface and to reproduce the Brownian motion that satisfies the fluctuation–dissipation theorem. The immersed boundary (IB) method [16] is an efficient way to apply the no-slip boundary condition on moving solid objects in a fixed Cartesian coordinate system. Many researchers have applied the IB method to the simulation of particulate flows [17–21]. The fluctuation–dissipation theorem can be satisfied by use of the Landau–Lifshitz Navier–Stokes (LLNS) equations in the fluctuating hydrodynamics [22,23], which includes the stochastic fluctuation stress. Several researchers have simulated the Brownian motion of colloidal particles by use of the LLNS as well as the IB method [24–27]. Secondly, an issue of the gas–liquid two-phase flow is to capture a free surface on which surface tension is exerted. The level set method [28] is one of the most reliable approaches to capture the free surface, because it enables us to calculate accurately the normal vectors and curvatures of the free surface, compared with other capturing methods [29–31]. Many researchers have applied the method to simulations of gas–liquid two-phase flows with phase change [32–37].

Although both colloidal suspension flows and two-phase flows with phase change have been successfully simulated, few direct simulations of the drying colloidal suspension have ever been presented in the literature. A difficulty with the simulation is modeling of the capillary force exerted on the particles protruding from a free surface. In Ref. [15], the capillary force is modeled as the simple spring force that is a function of the immersed height of the particle, in which the free surface is not deformed. In Ref. [14], the capillary force and the deformation of the free surface are calculated through the specified wettability parameter, in which the contact angle on the particle surface cannot be explicitly specified. Most recently, we have developed the immersed free surface (IFS) model to estimate accurately and efficiently capillary forces exerted on many particles at a free surface [38]. The IFS model is used along with the immersed boundary method and the level set method to accomplish a three-way coupling of the fluid flow, the free surface motion and the particle motion. This paper aims to develop a new direct simulation method for a drying colloidal suspension on a substrate using the IFS model. The present simulation method includes the crucial forces exerted on colloidal particles, such as the contact force, the van der Waals force, the electrostatic force, the capillary force, and the fluctuating hydrodynamic force, as shown in Fig. 1. Therefore, the present method enables us to estimate a variety of microstructures of colloidal particles on a substrate during drying.

This paper consists of the following parts. In Section 2, mathematical formulation in the present method is described. Namely, the governing equations of free surface motion, gas–liquid two-phase flow with phase change and particle motion are derived from the conservation laws. The IFS model is introduced into the equation of the free surface motion. In Section 3, numerical solver is described, in which the solution algorithm and the discretization of the governing equations are given in detail. In Section 4, some simulation results are illustrated to stress the capability of the present method. All the simulations in this paper are applied to gas–liquid two-phase flows with density ratio of 1000. Finally, the conclusion of this paper is stated in Section 5.

2. Mathematical formulation

A gas–liquid–solid three phase flow is considered in this paper, in which a liquid and its vapor, spherical solid particles and a substrate exist. Fig. 2 shows a two-dimensional schematic picture of the flow field on a Cartesian grid modeled in the present simulation method. The gas–liquid two-phase flow is treated as a single-field model, in which one set of conservation equations with the variable density and the variable viscosity is adopted. The free surface has a finite thickness, in which the density and the viscosity changes continuously. Each spherical particle is treated as a rigid body, in
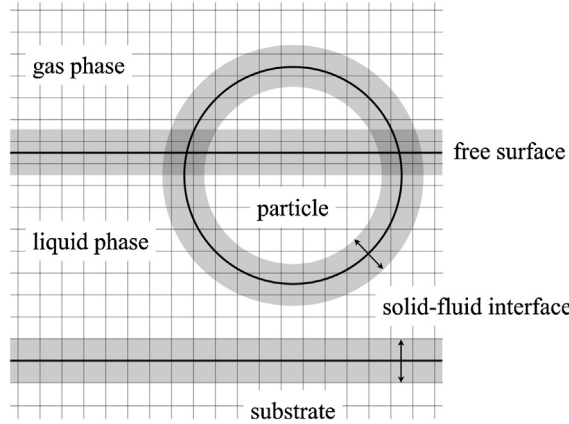
Fig. 2. A two-dimensional schematic picture of the flow field on a Cartesian grid modeled in the present simulation method. The upper thick line represents the sharp interface between gas and liquid. The lower thick line represents the sharp interface between liquid and solid. The thick circle represents the sharp interface between solid and fluid.
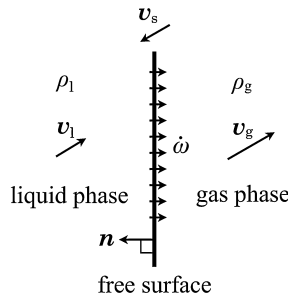
Fig. 3. A schematic picture of flow across a free surface. $\boldsymbol{v}_l$ is the velocity of liquid phase, $\boldsymbol{v}_g$ is the velocity of gas phase, $\boldsymbol{v}_s$ is the velocity of free surface, ρ_l is the density of liquid phase, ρ_g is the density of gas phase, $\dot{\omega}$ is the vaporization mass flow rate per unit surface and $\boldsymbol{n}$ is the unit normal to the free surface toward the liquid phase.

which the particle motion has 6 degrees of freedom: 3 for translation and 3 for rotation. The interface between the solid phase (particle and substrate) and the fluid has a finite thickness to accomplish the solid–fluid coupling in the IB method.

2.1. Free surface motion: level set method

Fig. 3 shows a schematic picture of flow across a free surface. The mass conservation law between the liquid phase and the gas phase is expressed as

$$\rho_l(\boldsymbol{v}_s - \boldsymbol{v}_l) \cdot \boldsymbol{n} = \rho_g(\boldsymbol{v}_s - \boldsymbol{v}_g) \cdot \boldsymbol{n} = (1 - \Psi)\dot{\omega}, \tag{1}$$

where Ψ is the total fraction of solid phase that is introduced to eliminate the phase change in the solid phase. The velocity of the free surface leads to

$$\boldsymbol{v}_s = \boldsymbol{v}_l + (1 - \Psi)\frac{\dot{\omega}}{\rho_l}\boldsymbol{n} = \boldsymbol{v}_g + (1 - \Psi)\frac{\dot{\omega}}{\rho_g}\boldsymbol{n}. \tag{2}$$

Then the velocity of the free surface can be expressed in a single-field model as

$$\boldsymbol{v}_s = \boldsymbol{v} + (1 - \Psi)\frac{\dot{\omega}}{\rho}\boldsymbol{n}, \tag{3}$$

where $\boldsymbol{v}$ and ρ are the velocity and the variable density of fluid, respectively. Using the level set (LS) method [28], a free surface is defined as the zero level surface of a level set function ϕ. The advection equation of ϕ is given by

$$\frac{\partial \phi}{\partial t} + \boldsymbol{v}_s \cdot \nabla \phi = 0, \tag{4}$$

where the domain of $\phi > 0$ represents the liquid phase and the domain of $\phi < 0$ represents the gas phase. The reinitialization of the level set function is accomplished using a converged solution of the advection equation as

$$\frac{\partial \phi}{\partial \tau} + S(\phi_0)\boldsymbol{n} \cdot \nabla \phi = S(\phi_0), \tag{5}$$
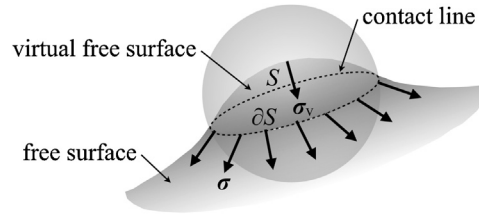
Fig. 4. A schematic picture of the immersed free surface (IFS) model for a particle on a free surface. S is the virtual free surface in the particle and ∂S is the contact line. σ is the surface tension exerted on the contact line and σ_v is the net surface tension exerted on the virtual free surface.

where

$$S(\phi_0) = \begin{cases} 0 & |\phi_0| \leq \frac{1}{2}h \\ \frac{\phi_0}{\sqrt{\phi_0{}^2 + h^2}} & |\phi_0| > \frac{1}{2}h \end{cases} \tag{6}$$

is the modified sign function [39], τ is the pseudo time step, ϕ_0 is the level set function before the reinitialization and h is the grid spacing. The unit normal vector to the free surface toward the liquid phase is given by

$$\boldsymbol{n} = \frac{\nabla \phi}{|\nabla \phi|}. \tag{7}$$

In addition, the fraction of liquid phase is calculated from the level set function using a smoothed Heaviside function as

$$F = \begin{cases} 0 & \phi < -\alpha \\ \frac{1}{2\pi} \sin \frac{\pi \phi}{\alpha} + \frac{\phi}{2\alpha} + \frac{1}{2} & -\alpha \leq \phi \leq \alpha \\ 1 & \phi > \alpha, \end{cases} \tag{8}$$

where $\alpha = 1.5h$ represents the half thickness of the free surface.

It is generally required to solve the transport equations of energy and vapor to estimate the vaporization mass flow rate per unit surface $\dot{\omega}$, because $\dot{\omega}$ is the function of the mass fraction of vapor species and temperature at the free surface [40]. During drying of a colloidal suspension, $\dot{\omega}$ may change in space and in time. Nevertheless, a constant $\dot{\omega}$ is used in this paper, because the focus of this paper is not to reproduce the behavior of phase change but to simulate the interactions between colloidal particles and a moving free surface. Therefore, the simulation results that are insensitive to a change of $\dot{\omega}$ are illustrated in this paper. Actually, a constant $\dot{\omega}$ could be an acceptable assumption, if the deformation of a free surface would be small enough for the diffusion of the vapor to be assumed constant in space.

2.2. Virtual free surface: immersed free surface model

Most recently, we have proposed the immersed free surface (IFS) model [38], in which a free surface is extended into the solid phase as a virtual free surface that is smoothly connected to the free surface at the three-phase contact line. Fig. 4 shows a schematic picture of the IFS model for a particle on a free surface. The total surface tension exerted on the contact line is replaced with the total surface tension exerted on the virtual free surface as

$$\oint_{\partial S} \sigma \, dr = \int_S \sigma_v \, ds. \tag{9}$$

A proof in two dimensions of Eq. (9) is described in Ref. [38]. Furthermore, the total surface tension exerted on the virtual free surface is transformed into the body force using the continuous surface force (CSF) model [41]. In a word, the force and the torque exerted on a solid phase are obtained from the volume integration of the body force in the solid phase instead of the line integration of the surface tension at the contact line. The transformation from the line integration into the volume integration leads to great savings of computational effort, because we do not have to define the contact line on the surface of solid phase. The shape of the virtual free surface may be arbitrary if the following conditions are satisfied. Firstly, the virtual free surface is required to intersect with the solid–fluid interface at a specified contact angle. Secondly, the whole virtual free surface is required to be inside the solid phase. To satisfy the above conditions, the level set function is modified in the l-th solid-phase using the advection equation as

$$\frac{\partial \phi}{\partial \tau} + \Psi \boldsymbol{e}_l \cdot \nabla \phi = \Psi |\nabla \phi| \cos \theta_l, \tag{10}$$

where $\boldsymbol{e}_l$ is the inward unit normal to the l-th solid phase and θ_l is the specified contact angle at the surface of the l-th solid phase. At each time step, the level set function in the solid-phase is modified using Eq. (10) after solving Eq. (4) in

the whole domain. The equation is solved in an iterative manner as well as Eq. (5). The converged solution of Eq. (10) is expressed at the surface of the *l*-th solid phase as

$$\boldsymbol{e}_l \cdot \boldsymbol{n} = \cos \theta_l, \tag{11}$$

which means that the free surface intersects with the surface of the *l*-th solid phase at the specified contact angle. The modification of the level set function in the solid phase is followed by the reinitialization of the level set function in the whole domain.

Due to the above modification, the total volume of liquid phase is prone to be erroneous. Therefore, a simple correcting method of the level set function is introduced to conserve the total volume of liquid phase. After the reinitialization, the level set function is corrected as

$$\phi = \phi_e - \frac{\Delta V}{S_s}, \tag{12}$$

where ϕ_e is the erroneous level set function, ΔV is the volumetric error of liquid phase between before and after solving the level set equations and S_s is the area of free surface. The area of free surface is given by

$$S_s = \int_{\Omega} (1 - \Psi) \frac{\partial F}{\partial \phi} dx dy dz, \tag{13}$$

where Ω is the whole computational domain. The volumetric error of liquid phase is expressed as

$$\Delta V = V^{\text{after}} - \left(V^{\text{before}} - E \right), \tag{14}$$

where V^{before} is the volume of liquid phase before solving the level set equations, V^{after} is the volume of liquid phase after solving the level set equations and E is the phase change volume of liquid phase at each time step. The volume of liquid phase is given by

$$V = \int_{\Omega} (1 - \Psi) F dx dy dz, \tag{15}$$

and the phase change volume of liquid phase at each time step is given by

$$E = \frac{\dot{\omega}}{\rho_l} S_s \Delta t, \tag{16}$$

where Δt is the computational time step. The above correction means a parallel translation of the level set function, so that it does not impair the property of the distance function ϕ. It is noted that Eq. (12) may be only valid for such a simple topology of the liquid phase that will be presented in this paper. We are planning to introduce a more sophisticated method to correct the level set function that is applicable to a complicated topology of the liquid phase.

2.3. Multiphase flow: immersed boundary method

The law of mass conservation of multiphase flow is expressed as

$$\frac{\partial \rho}{\partial t} + \nabla \cdot (\rho \boldsymbol{v}) = 0. \tag{17}$$

To employ a pressure-based solver, the continuity equation is derived from Eq. (4) and Eq. (17) as follows: multiplying Eq. (4) by $\partial \rho / \partial \phi$ and substituting $\boldsymbol{n} = \nabla \rho / |\nabla \rho|$ yields

$$\frac{\partial \rho}{\partial t} + \nabla \cdot (\rho \boldsymbol{v}) - \rho \nabla \cdot \boldsymbol{v} + \frac{(1 - \Psi) \dot{\omega}}{\rho} |\nabla \rho| = 0. \tag{18}$$

Comparing Eq. (18) with Eq. (17), a non-conservative form of the continuity equation is given as

$$\nabla \cdot \boldsymbol{v} = \frac{(1 - \Psi) \dot{\omega}}{\rho^2} |\nabla \rho|. \tag{19}$$

Eq. (19) is rewritten in a conservative form as

$$\nabla \cdot \boldsymbol{v} = (1 - \Psi) \dot{\omega} \left| \nabla \left(\frac{1}{\rho} \right) \right|, \tag{20}$$

which is adopted in the present method. The velocity jump condition at the free surface induced by phase change is naturally imposed through the continuity equation of Eq. (20). In a free surface with finite thickness, the smoothly varying density of fluid yields a non-zero divergence of velocity. As a result, the velocity jump takes place across the free surface with phase change.

The law of momentum conservation is based on the Landau–Lifshitz Navier–Stokes (LLNS) equations and expressed as

$$\rho \frac{\partial \boldsymbol{v}}{\partial t} = -\rho \boldsymbol{v} \cdot \nabla \boldsymbol{v} - \nabla p + \nabla \cdot \mu \left\{ \nabla \boldsymbol{v} + (\nabla \boldsymbol{v})^T \right\} - \frac{2}{3} \nabla \cdot \left\{ \mu (\nabla \cdot \boldsymbol{v}) \boldsymbol{I} \right\}$$
$$+ \nabla \cdot \boldsymbol{S} + \rho \boldsymbol{g} + \boldsymbol{F}_s + \boldsymbol{F}_p, \tag{21}$$

where p is the pressure, μ is the variable viscosity of fluid, $\boldsymbol{I}$ is the identity matrix, $\boldsymbol{S}$ is the stochastic stress tensor, $\boldsymbol{g}$ is the gravity acceleration, $\boldsymbol{F}_s$ is the surface tension, and $\boldsymbol{F}_p$ is the body force that is introduced for solid–fluid coupling in the immersed boundary (IB) method [17]. Note that the fourth term in the right-hand side cannot be eliminated, because the divergence of velocity is not equal to zero for a flow with variable density. The variable density and the variable viscosity are given by

$$\rho = F \rho_l + (1 - F) \rho_g, \tag{22}$$

$$\mu = F \mu_l + (1 - F) \mu_g, \tag{23}$$

where μ_l is the viscosity of liquid phase, μ_g is the viscosity of gas phase.

The stochastic stress tensor [42] is given by

$$\boldsymbol{S} = \begin{bmatrix} s_{xx} & s_{xy} & s_{xz} \\ s_{yx} & s_{yy} & s_{yz} \\ s_{zx} & s_{zy} & s_{zz} \end{bmatrix}, \tag{24}$$

where

$$\langle s_{xx} \rangle = \langle s_{xy} \rangle = \langle s_{xz} \rangle = \langle s_{yx} \rangle = \langle s_{yy} \rangle = \langle s_{yz} \rangle = \langle s_{zx} \rangle = \langle s_{zy} \rangle = \langle s_{zz} \rangle = 0,$$

$$\langle s_{xx}^2 \rangle = \langle s_{yy}^2 \rangle = \langle s_{zz}^2 \rangle = \frac{8}{3} k_B T \mu \delta(x - x') \delta(y - y') \delta(z - z') \delta(t - t'),$$

$$\langle s_{xx} s_{yy} \rangle = \langle s_{xx} s_{zz} \rangle = \langle s_{yy} s_{zz} \rangle = -\frac{4}{3} k_B T \mu \delta(x - x') \delta(y - y') \delta(z - z') \delta(t - t'),$$

$$\langle s_{xy}^2 \rangle = \langle s_{xz}^2 \rangle = \langle s_{yz}^2 \rangle = 2 k_B T \mu \delta(x - x') \delta(y - y') \delta(z - z') \delta(t - t'),$$

$$\langle s_{yx}^2 \rangle = \langle s_{xy}^2 \rangle, \quad \langle s_{zx}^2 \rangle = \langle s_{xz}^2 \rangle, \quad \langle s_{zy}^2 \rangle = \langle s_{yz}^2 \rangle. \tag{25}$$

Here $\langle \rangle$ denotes an ensemble average, k_B is the Boltzmann constant, T is the temperature and δ is the Dirac's delta function. The surface tension is expressed according to the CSF model as

$$\boldsymbol{F}_s = \sigma \kappa \nabla F, \tag{26}$$

where σ is the surface tension coefficient, κ is the mean curvature of free surface that is calculated from the level set function [43] as

$$\kappa = -\nabla \cdot \boldsymbol{n} = -\frac{1}{(\phi_x^2 + \phi_y^2 + \phi_z^2)^{3/2}} \left(\phi_x^2 \phi_{yy} - 2\phi_x \phi_y \phi_{xy} + \phi_y^2 \phi_{xx} + \phi_x^2 \phi_{zz} - 2\phi_x \phi_z \phi_{xz} + \phi_z^2 \phi_{xx} \right.$$
$$\left. + \phi_y^2 \phi_{zz} - 2\phi_y \phi_z \phi_{yz} + \phi_z^2 \phi_{yy} \right). \tag{27}$$

The body force is expressed as

$$\boldsymbol{F}_p = \Psi \rho \frac{\boldsymbol{v}_p - \boldsymbol{v}}{\Delta t}, \tag{28}$$

where $\boldsymbol{v}_p$ is the total velocity of solid phase. This simple immersed boundary method may have such numerical problems as temporal oscillation, grid dependency and velocity divergence [44]. From our experience, however, those problems are practically unnoticeable for a particulate flow of low Reynolds number that contains the particles heavier than the fluid. It is probably because the inertia effect is very small. In fact, the particle Reynolds number is at most 0.05 in the present simulations. The total fraction of solid phase is a summation of the fractions of the solid phases (particles and substrate) that overlap one another as

$$\Psi = \sum_l \psi_l, \tag{29}$$

where ψ_l is the fraction of the l-th solid phase. Here ψ_l is calculated using a smoothed Heaviside function as

$$\psi_l = \begin{cases} 0 & d_l < -\alpha \\ \frac{1}{2\pi} \sin \frac{\pi d_l}{\alpha} + \frac{d_l}{2\alpha} + \frac{1}{2} & -\alpha \leq d_l \leq \alpha \\ 1 & d_l > \alpha, \end{cases} \tag{30}$$

where d_l is the signed distance function from the l-th solid–fluid interface and $\alpha = 1.5h$ is the half thickness of the solid–fluid interface. For a spherical particle, d_l is given by

$$d_l = a_l - |\bar{\boldsymbol{r}}_l|, \tag{31}$$

where a_l is the radius of the l-th particle and $\bar{\boldsymbol{r}}_l$ is the position vector from the center of the l-th particle. The total velocity of solid phase is a weighted average of the rigid velocities of the solid phases that overlap one another as

$$\boldsymbol{v}_{\mathrm{p}} = \frac{\sum_l \psi_l \boldsymbol{v}_{\mathrm{p},l}}{\sum_l \psi_l}, \tag{32}$$

where $\boldsymbol{v}_{\mathrm{p},l}$ is the rigid velocity of the l-th solid phase. For a spherical particle,

$$\boldsymbol{v}_{\mathrm{p},l} = \boldsymbol{V}_l + \boldsymbol{\Omega}_l \times \bar{\boldsymbol{r}}_l, \tag{33}$$

where $\boldsymbol{V}_l$ is the translational velocity of the l-th particle and $\boldsymbol{\Omega}_l$ is the rotational velocity of the l-th particle. The body force works only in the solid phase, in which the velocity in Eq. (21) is forced into the total velocity of solid phase. As a result, the no-slip boundary condition on the solid–fluid interface is implicitly fulfilled.

2.4. Particles: Newtonian dynamics

Based on the Newton's second law of motion. The translational motion of the l-th particle is expressed as

$$M_l \frac{d\boldsymbol{V}_l}{dt} = \boldsymbol{F}_{\mathrm{c},l} + \boldsymbol{F}_{\mathrm{e},l} + \boldsymbol{F}_{\mathrm{v},l} + \boldsymbol{F}_{\mathrm{h},l}, \tag{34}$$

where M_l is the mass of particle, $\boldsymbol{F}_{\mathrm{c},l}$ is the contact force, $\boldsymbol{F}_{\mathrm{e},l}$ is the electrostatic force, $\boldsymbol{F}_{\mathrm{v},l}$ is the van der Waals force and $\boldsymbol{F}_{\mathrm{v},l}$ is the hydrodynamic force. The rotational motion of the l-th particle is expressed as

$$I_l \frac{d\boldsymbol{\Omega}_l}{dt} = \boldsymbol{T}_{\mathrm{c},l} + \boldsymbol{T}_{\mathrm{h},l}, \tag{35}$$

where I_l is the inertia moment of particle, $\boldsymbol{T}_{\mathrm{c},l}$ is the contact torque and $\boldsymbol{T}_{\mathrm{h},l}$ is the hydrodynamic torque. The trajectory of the l-th particle is calculated from the translational velocity as

$$\frac{d\boldsymbol{X}_l}{dt} = \boldsymbol{V}_l, \tag{36}$$

where $\boldsymbol{X}_l$ denotes the center of the l-th particle.

The contact force and the contact torque are obtained by a summation of the forces exerted by solid objects (particles and substrate) that are in contact with the l-th particle as

$$\boldsymbol{F}_{\mathrm{c},l} = \sum_m (\boldsymbol{f}_{\mathrm{n},m} + \boldsymbol{f}_{\mathrm{t},m}), \tag{37}$$

$$\boldsymbol{T}_{\mathrm{c},l} = a_l \sum_m (\boldsymbol{n}_m \times \boldsymbol{f}_{\mathrm{t},m}). \tag{38}$$

Here m is an index of the solid object that is in contact with the l-th particle, $\boldsymbol{f}_{\mathrm{n},m}$ is the normal force exerted by the m-th solid object, $\boldsymbol{f}_{\mathrm{t},m}$ is the tangential force exerted by the m-th solid object and $\boldsymbol{n}_m$ is the unit normal vector to the m-th solid object. The normal force and the tangential force are given by the Voigt model [45] used in the discrete element method (DEM) [46]. The tangential force consists of a slider as well as a spring and a dashpot, so that the model is able to describe a friction between solid objects. The reason why we adopt this sophisticated model is that the frictions of particle-to-particle and particle-to-substrate play a crucial role for a structure formation of the colloidal particles [47,48]. The Voigt model is described in our previous work on a DEM simulation [49] in detail.

The electrostatic force and the van der Waals force are obtained by a summation of the forces exerted by solid objects that are close to the l-th particle as

$$\boldsymbol{F}_{\mathrm{e},l} + \boldsymbol{F}_{\mathrm{v},l} = \sum_m (-f_{\mathrm{e},m} + f_{\mathrm{v},m}) \boldsymbol{n}_m, \tag{39}$$

where m is an index of the solid object close to the particle, $f_{\mathrm{e},m}$ is the magnitude of two-body electrostatic force and $f_{\mathrm{v},m}$ is the magnitude of two-body van der Waals force. Both the two-body electrostatic force and the two-body van der Waals force are given by the DLVO (Derjaguin–Landau–Verwey–Overbeek) theory [50]. The magnitudes of the forces are functions of the inter-surface distance between two solid objects. If the electric charges on the two solid objects have the same sign, the electrostatic force is repulsive. On the other hand, the van der Waals force is always attractive. The formulae of the two-body forces are described in Ref. [49] in detail. It is noted that the surface of solid object is treated as a sharp interface to estimate $\boldsymbol{F}_{\mathrm{c},l}$, $\boldsymbol{T}_{\mathrm{c},l}$, $\boldsymbol{F}_{\mathrm{e},l}$ and $\boldsymbol{F}_{\mathrm{v},l}$, unlike the hydrodynamic force and the hydrodynamic torque described below.
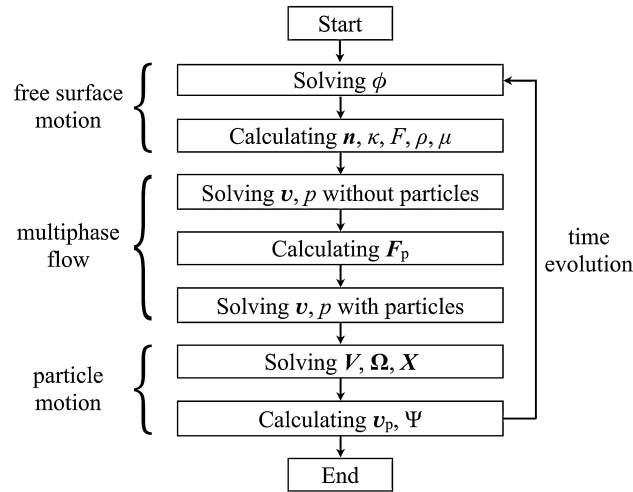
Fig. 5. Solution algorithm in the present simulation method.

The hydrodynamic force and the hydrodynamic torque are obtained by the volume integration of the body force in Eq. (28) as

$$\boldsymbol{F}_{h,l} = -\int \{\boldsymbol{F}_p - \Psi(\rho_p - \rho)\boldsymbol{g}\}dV,$$ (40)

$$\boldsymbol{T}_{h,l} = -\int (\bar{\boldsymbol{r}}_l \times \boldsymbol{F}_p)dV,$$ (41)

where ρ_p is the density of particle. As shown in Eq. (40), the buoyancy is included in the hydrodynamic force. Using the immersed free surface model, the capillary force and the capillary torque exerted on the particle are naturally introduced into $\boldsymbol{F}_{h,l}$ and $\boldsymbol{T}_{h,l}$, respectively. This is because $\boldsymbol{F}_p$ is a function of $\boldsymbol{v}$ in the particle that is induced by the surface tension exerted on the virtual free surface. Then we can compute efficiently the capillary force exerted on a particle by the present method, because any explicit treatment of the contact angle boundary condition is not necessary. Furthermore, it is noted that $\boldsymbol{F}_h$ and $\boldsymbol{T}_h$ are stochastic because $\boldsymbol{F}_p$ is a function of fluctuating velocity $\boldsymbol{v}$. Then the translational and the rotational Brownian motions of the particle emanate from the above stochastic hydrodynamic force and torque.

3. Numerical solver

The present simulation method employs a weakly-coupled numerical solver for gas–liquid–solid three-phase flows. In a word, the equations of free surface motion, multiphase flow and particle motion are solved in sequence at each time step. Fig. 5 shows the solution algorithm in the present simulation method in a flow chart. Major discretization schemes to solve the equations are described in the following subsections.

3.1. Solving free surface motion: TVD Runge–Kutta and WENO scheme

The free surface and the virtual free surface are represented by the level set function. The equations of the level set function, Eqs. (4), (5) and (10) must be solved accurately, especially for gas–liquid two-phase flows with high density ratios. Therefore, a third-order total variation diminishing (TVD) Runge–Kutta scheme [51] and a fifth-order weighted essentially non-oscillatory (WENO) scheme [52] are adopted to solve the equations in this paper. These schemes allow us to simulate gas–liquid two-phase flows with density ratio up to 1000. All the variables in the level set equations are defined at cell centers. Expressing the right-hand side of the equations as $R(\phi)$, a third-order TVD Runge–Kutta scheme is expressed as

$$\phi_{i,j,k}^* = \phi_{i,j,k}^n + \Delta t R(\phi_{i,j,k}^n),$$
$$\phi_{i,j,k}^{**} = \frac{3}{4}\phi_{i,j,k}^n + \frac{1}{4}\{\phi_{i,j,k}^* + \Delta t R(\phi_{i,j,k}^*)\},$$
$$\phi_{i,j,k}^{n+1} = \frac{1}{3}\phi_{i,j,k}^n + \frac{2}{3}\{\phi_{i,j,k}^{**} + \Delta t R(\phi_{i,j,k}^{**})\},$$ (42)

where n and $n + 1$ are indices for temporal discretization. The right-hand side of the level set equations has a uniform expression as

$$R(\phi_{i,j,k}) = -(\hat{u}_{i,j,k}\phi_{x,i,j,k} + \hat{v}_{i,j,k}\phi_{y,i,j,k} + \hat{w}_{i,j,k}\phi_{z,i,j,k}) + \hat{H}_{i,j,k},$$ (43)

where $\hat{u}_{i,j,k}$, $\hat{v}_{i,j,k}$, $\hat{w}_{i,j,k}$ are the components of the advection velocity and $\hat{H}_{i,j,k}$ is the source term. Note that i, j, k are indices for spatial discretization. Using an upstream differencing scheme, the advection term in x direction is discretized as

$$\hat{u}_{i,j,k}\phi_{x,i,j,k} = \frac{\hat{u}_{i,j,k} - |\hat{u}_{i,j,k}|}{2}\phi_{x,i}^+ + \frac{\hat{u}_{i,j,k} + |\hat{u}_{i,j,k}|}{2}\phi_{x,i}^-, \tag{44}$$

where $\phi_{x,i}^+$ represents a forward differencing and $\phi_{x,i}^-$ represents a backward differencing, respectively. The advection terms in y and z directions are discretized in the same manner.

In the fifth-order WENO scheme, the forward differencing and the backward differencing are expressed as weighted averages of three third-order differencing schemes as

$$\phi_{x,i}^{\pm} = \omega_{x,i}^{\pm,1}\phi_{x,i}^{\pm,1} + \omega_{x,i}^{\pm,2}\phi_{x,i}^{\pm,2} + \omega_{x,i}^{\pm,3}\phi_{x,i}^{\pm,3}, \tag{45}$$

where $\omega_{x,i}^{\pm,m}$ is the weighting coefficients. The third-order differencing schemes are expressed as

$$\phi_{x,i}^{\pm,1} = \frac{d_{x,i}^{\pm,1}}{3} - \frac{7d_{x,i}^{\pm,2}}{6} + \frac{11d_{x,i}^{\pm,3}}{6},$$

$$\phi_{x,i}^{\pm,2} = -\frac{d_{x,i}^{\pm,2}}{6} + \frac{5d_{x,i}^{\pm,3}}{6} + \frac{d_{x,i}^{\pm,4}}{3},$$

$$\phi_{x,i}^{\pm,3} = \frac{d_{x,i}^{\pm,3}}{3} + \frac{5d_{x,i}^{\pm,4}}{6} - \frac{d_{x,i}^{\pm,5}}{6}, \tag{46}$$

where $d_{x,i}^{\pm,m}$ is the first-order differencing scheme defined as

$$d_{x,i}^{\pm,m} = \pm\frac{\phi_{i\pm(4-m),j,k} - \phi_{i\pm(3-m),j,k}}{\Delta x}. \tag{47}$$

Here Δx denotes the grid spacing in x direction. Each weighting coefficient is expressed as

$$\omega_{x,i}^{\pm,m} = \frac{\alpha_{x,i}^{\pm,m}}{\sum_{m=1}^3 \alpha_{x,i}^{\pm,m}}, \tag{48}$$

where

$$\alpha_{x,i}^{\pm,1} = \frac{0.1}{(S_{x,i}^{\pm,1} + \epsilon)^2}, \qquad \alpha_{x,i}^{\pm,1} = \frac{0.6}{(S_{x,i}^{\pm,2} + \epsilon)^2}, \qquad \alpha_{x,i}^{\pm,1} = \frac{0.3}{(S_{x,i}^{\pm,3} + \epsilon)^2}. \tag{49}$$

Here $\epsilon = 10^{-10}$ is a small value to avoid dividing by zero and $S_{x,i}^{\pm,m}$ is the smoothness indicator of each third-order differencing as

$$S_{x,i}^{\pm,1} = \frac{13}{12}(d_{x,i}^{\pm,1} - 2d_{x,i}^{\pm,2} + d_{x,i}^{\pm,3})^2 + \frac{1}{4}(d_{x,i}^{\pm,1} - 4d_{x,i}^{\pm,2} + 3d_{x,i}^{\pm,3})^2,$$

$$S_{x,i}^{\pm,2} = \frac{13}{12}(d_{x,i}^{\pm,2} - 2d_{x,i}^{\pm,3} + d_{x,i}^{\pm,4})^2 + \frac{1}{4}(d_{x,i}^{\pm,2} - d_{x,i}^{\pm,4})^2,$$

$$S_{x,i}^{\pm,3} = \frac{13}{12}(d_{x,i}^{\pm,3} - 2d_{x,i}^{\pm,4} + d_{x,i}^{\pm,5})^2 + \frac{1}{4}(3d_{x,i}^{\pm,3} - 4d_{x,i}^{\pm,4} + d_{x,i}^{\pm,5})^2. \tag{50}$$

The advection velocity and the source term in Eq. (43) depend on each equation of the level set function. For the advection equation of Eq. (4),

$$\hat{u}_{i,j,k} = \bar{u}_{i,j,k} + \frac{(1 - \Psi_{i,j,k})\dot{\omega}}{\rho_{i,j,k}}n_{x,i,j,k},$$

$$\hat{v}_{i,j,k} = \bar{v}_{i,j,k} + \frac{(1 - \Psi_{i,j,k})\dot{\omega}}{\rho_{i,j,k}}n_{y,i,j,k},$$

$$\hat{w}_{i,j,k} = \bar{w}_{i,j,k} + \frac{(1 - \Psi_{i,j,k})\dot{\omega}}{\rho_{i,j,k}}n_{z,i,j,k},$$

$$\hat{H}_{i,j,k} = 0, \tag{51}$$

where n_x, n_y, n_z are the components of $\boldsymbol{n}$ as

$$n_{x,i,j,k} = \frac{\phi_{x,i,j,k}}{\sqrt{\phi_{x,i,j,k}^2 + \phi_{y,i,j,k}^2 + \phi_{z,i,j,k}^2}},$$

$$n_{y,i,j,k} = \frac{\phi_{y,i,j,k}}{\sqrt{\phi_{x,i,j,k}^2 + \phi_{y,i,j,k}^2 + \phi_{z,i,j,k}^2}},$$

$$n_{z,i,j,k} = \frac{\phi_{z,i,j,k}}{\sqrt{\phi_{x,i,j,k}^2 + \phi_{y,i,j,k}^2 + \phi_{z,i,j,k}^2}}. \tag{52}$$

Here derivatives ϕ_x, ϕ_y, ϕ_z are obtained using the second-order central differencing. In addition, $\bar{u}$, $\bar{v}$, $\bar{w}$ in Eq. (51) are the components of cell-centered flow velocity. Since the flow velocity is defined at cell faces on a staggered grid, the cell-centered velocity should be estimated using the cell-faced velocity. In the present method, it is achieved based on the assumption that a cell face is occupied by the fluid with larger density between both sides of the cell face. According to this assumption, the components of the cell-centered velocity are expressed as

$$\bar{u}_{i,j,k} = \begin{cases} u_{i,j,k} & n_{x,i,j,k} \geq 0 \\ u_{i+1,j,k} & n_{x,i,j,k} < 0, \end{cases}$$

$$\bar{v}_{i,j,k} = \begin{cases} v_{i,j,k} & n_{y,i,j,k} \geq 0 \\ v_{i,j+1,k} & n_{y,i,j,k} < 0, \end{cases}$$

$$\bar{w}_{i,j,k} = \begin{cases} w_{i,j,k} & n_{z,i,j,k} \geq 0 \\ w_{i,j,k+1} & n_{z,i,j,k} < 0. \end{cases} \tag{53}$$

For the reinitialization equation of Eq. (5), the advection velocity and the source term are expressed as

$$\hat{u}_{i,j,k} = S(\phi_{0,i,j,k})n_{x,i,j,k},$$

$$\hat{v}_{i,j,k} = S(\phi_{0,i,j,k})n_{y,i,j,k},$$

$$\hat{w}_{i,j,k} = S(\phi_{0,i,j,k})n_{z,i,j,k},$$

$$\hat{H}_{i,j,k} = S(\phi_{0,i,j,k}), \tag{54}$$

where $S(\phi_{0,i,j,k})$ is the discretized form of Eq. (6). For the modification equation of Eq. (10),

$$\hat{u}_{i,j,k} = \Psi_{i,j,k} \frac{\sum_l \psi_{l,i,j,k} e_{l,x,i,j,k}}{\sum_l \psi_{l,i,j,k}},$$

$$\hat{v}_{i,j,k} = \Psi_{i,j,k} \frac{\sum_l \psi_{l,i,j,k} e_{l,y,i,j,k}}{\sum_l \psi_{l,i,j,k}},$$

$$\hat{w}_{i,j,k} = \Psi_{i,j,k} \frac{\sum_l \psi_{l,i,j,k} e_{l,z,i,j,k}}{\sum_l \psi_{l,i,j,k}},$$

$$\hat{H}_{i,j,k} = \Psi_{i,j,k} \frac{\sum_l \psi_{l,i,j,k} \theta_l}{\sum_l \psi_{l,i,j,k}}, \tag{55}$$

where $e_{l,x}$, $e_{l,y}$, $e_{l,z}$ are the components of $\boldsymbol{e}_l$. In a word, the normal vector and the contact angle are given by a linear combination of those of the overlapped solid phases.

The advection equation of the level set function is evolved with an actual time step Δt that is used in the multiphase flow computation. On the other hand, the reinitialization equation and the modification equation of the level set function are evolved with a pseudo time step $\Delta \tau$ that is decided under the condition of a numerical stability. If a smaller time step is used, the number of iterations N required for a convergence is increased. We use typically $\Delta \tau = 0.5h$ and $N = 10$ for both equations in this paper.

3.2. Curvature estimation: virtual grid differencing

For surface tension-dominated flows, an imbalance between the surface tension on the free surface and the pressure gradient across the free surface leads to unphysical flows (spurious flows) around the free surface. Many researchers have ever proposed accurate methods of curvature estimation to fix the problem [53–57]. A common principle in those methods is that a curvature at a cell is estimated at the foot of a perpendicular from the cell to the sharp interface between gas and liquid. Holding the principle, the curvatures in a free surface remain constant, which is crucial for the balance between the surface tension and the pressure gradient. In this paper, the foot of a perpendicular is obtained by the following method, which is similar to and simpler than the method in Ref. [57]. Fig. 6 shows a two-dimensional schematic picture
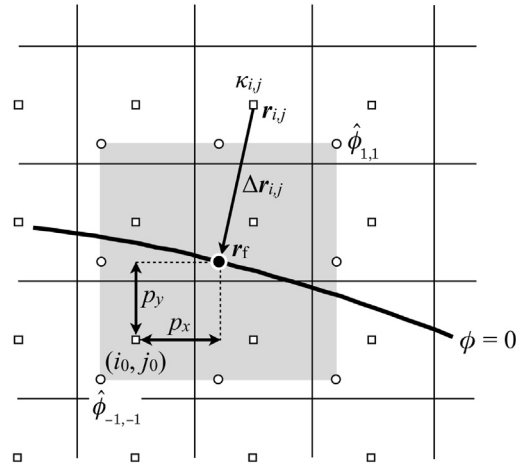
Fig. 6. A two-dimensional schematic picture of the present way of curvature estimation. The thick solid curve represents the sharp interface between gas and liquid of $\phi = 0$. The solid circle (●) represents the foot of perpendicular from the cell center (i, j) to the sharp interface. The foot is contained in the cell whose vertices are (i_0, j_0), $(i_0 + 1, j_0)$, $(i_0, j_0 + 1)$ and $(i_0 + 1, j_0 + 1)$. The location parameters in the foot-containing cell are given by p_x, p_y. The open circles (○) represent virtual grid points at which the level set functions $\hat{\phi}_{I,J}$ are interpolated.

of the present way of curvature estimation. Using the level set function and its normal, the position vector of the foot of perpendicular from the cell center to the sharp interface between gas and liquid is expressed as

$$\boldsymbol{r}_f = \boldsymbol{r}_{i,j,k} + \Delta \boldsymbol{r}_{i,j,k}, \tag{56}$$

where $\boldsymbol{r}_{i,j,k}$ is the position vector of a cell center and

$$\Delta \boldsymbol{r}_{i,j,k} = -\phi_{i,j,k} \boldsymbol{n}_{i,j,k}. \tag{57}$$

If a regular grid is used, the indices of the foot-containing cell is readily obtained as

$$i_0 = i - \text{int}\{1 - \text{sign}(0.5, \Delta r_{x,i,j,k})\} + \text{int}\left(\frac{\Delta r_{x,i,j,k}}{\Delta x}\right),$$

$$j_0 = j - \text{int}\{1 - \text{sign}(0.5, \Delta r_{y,i,j,k})\} + \text{int}\left(\frac{\Delta r_{y,i,j,k}}{\Delta y}\right),$$

$$k_0 = k - \text{int}\{1 - \text{sign}(0.5, \Delta r_{z,i,j,k})\} + \text{int}\left(\frac{\Delta r_{z,i,j,k}}{\Delta z}\right), \tag{58}$$

where i_0, j_0, k_0 are indices of the foot-containing cell, $\Delta r_{x,i,j,k}$, $\Delta r_{y,i,j,k}$, $\Delta r_{z,i,j,k}$ are the components of $\Delta \boldsymbol{r}_{i,j,k}$, int$(a)$ returns integer part of a and sign(a, b) returns the absolute value of a times the sign of b. The location of the foot is parameterized in the cell as

$$p_x = \text{mod}\left(\frac{\Delta r_{x,i,j,k}}{\Delta x}, 1\right) + 0.5 - \text{sign}(0.5, \Delta r_{x,i,j,k}),$$

$$p_y = \text{mod}\left(\frac{\Delta r_{y,i,j,k}}{\Delta y}, 1\right) + 0.5 - \text{sign}(0.5, \Delta r_{y,i,j,k}),$$

$$p_z = \text{mod}\left(\frac{\Delta r_{z,i,j,k}}{\Delta z}, 1\right) + 0.5 - \text{sign}(0.5, \Delta r_{z,i,j,k}), \tag{59}$$

where $0 \le p_x, p_y, p_z \le 1$ and mod(a, b) returns the remainder of the division of a by b.

In Ref. [57], the curvature at the foot is interpolated using the curvatures at vertices of the foot-containing cell. In this paper, on the other hand, the curvature at the foot is obtained by differencing the level set functions at 27 virtual grid points around the foot. The level set function at each virtual grid point is interpolated using the level set function at real grid points around the virtual grid point. In a word, differencing the interpolated level set function is substituted for interpolating the curvature obtained by differencing. This virtual grid differencing can lead to more accurate curvature estimation than Ref. [57], because the distribution of the level set function is smoother than the curvature distribution in general. The tri-linear interpolated level set functions at 27 virtual grid points are expressed as

$$\hat{\phi}_{I,J,K} = \phi_{i_0+I, j_0+J, k_0+K}(1 - p_x)(1 - p_y)(1 - p_z)$$
$$+ \phi_{i_0+I+1, j_0+J, k_0+K} p_x (1 - p_y)(1 - p_z)$$
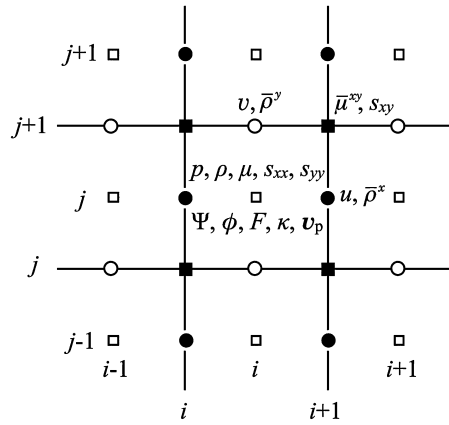
Fig. 7. A two-dimensional schematic picture of the flow variables on a staggered grid. p, ρ, μ, s_{xx}, s_{yy}, Ψ, ϕ, F, κ, $\boldsymbol{v}_{\mathrm{p}}$ are defined at cell centers (□). u, $\bar{\rho}^x$ are defined at cell faces in x direction (●). v, $\bar{\rho}^y$ are defined at cell faces in y direction (○). $\bar{\mu}^{xy}$, s_{xy} are defined at cell vertices (■).

$$+ \phi_{i_0+I, j_0+J+1, k_0+K}(1 - p_x)p_y(1 - p_z)$$
$$+ \phi_{i_0+I, j_0+J, k_0+K+1}(1 - p_x)(1 - p_y)p_z$$
$$+ \phi_{i_0+I+1, j_0+J+1, k_0+K}\,p_x p_y(1 - p_z)$$
$$+ \phi_{i_0+I+1, j_0+J, k_0+K+1}\,p_x(1 - p_y)p_z$$
$$+ \phi_{i_0+I, j_0+J+1, k_0+K+1}(1 - p_x)p_y p_z$$
$$+ \phi_{i_0+I+1, j_0+J+1, k_0+K+1}\,p_x p_y p_z, \tag{60}$$

where $I = -1, 0, 1$, $J = -1, 0, 1$ and $K = -1, 0, 1$. Then the curvature at the foot is calculated using Eq. (27). The derivatives in Eq. (27) are discretized by the standard second-order central differencing as

$$\phi_x = \frac{-\hat{\phi}_{-1,0,0} + \hat{\phi}_{1,0,0}}{2\Delta x}, \qquad \phi_y = \frac{-\hat{\phi}_{0,-1,0} + \hat{\phi}_{0,1,0}}{2\Delta y}, \qquad \phi_z = \frac{-\hat{\phi}_{0,0,-1} + \hat{\phi}_{0,0,1}}{2\Delta z},$$

$$\phi_{xx} = \frac{\hat{\phi}_{-1,0,0} - 2\hat{\phi}_{0,0,0} + \hat{\phi}_{1,0,0}}{\Delta x^2}, \qquad \phi_{yy} = \frac{\hat{\phi}_{0,-1,0} - 2\hat{\phi}_{0,0,0} + \hat{\phi}_{0,1,0}}{\Delta y^2},$$

$$\phi_{zz} = \frac{\hat{\phi}_{0,0,-1} - 2\hat{\phi}_{0,0,0} + \hat{\phi}_{0,0,1}}{\Delta z^2},$$

$$\phi_{xy} = \frac{\hat{\phi}_{-1,-1,0} - \hat{\phi}_{1,-1,0} - \hat{\phi}_{-1,1,0} + \hat{\phi}_{1,1,0}}{4\Delta x \Delta y},$$

$$\phi_{xz} = \frac{\hat{\phi}_{-1,0,-1} - \hat{\phi}_{1,0,-1} - \hat{\phi}_{-1,0,1} + \hat{\phi}_{1,0,1}}{4\Delta x \Delta z},$$

$$\phi_{yz} = \frac{\hat{\phi}_{0,-1,-1} - \hat{\phi}_{0,1,-1} - \hat{\phi}_{0,-1,1} + \hat{\phi}_{0,1,1}}{4\Delta y \Delta z}. \tag{61}$$

Finally, the curvature obtained above is used as the cell-centered curvature $\kappa_{i,j,k}$.

3.3. Solving multiphase flow: SMAC method with IB method

The governing equations of multiphase flow are spatially discretized on a staggered grid system. Fig. 7 shows a two-dimensional schematic picture of the flow variables on a staggered grid. For the temporally discretization, a time-splitting scheme is adopted to use the IB method. Firstly, a gas–liquid two phase flow without solid phase is obtained by solving Eq. (21) without $\boldsymbol{F}_{\mathrm{p}}$ as

$$\frac{\partial \tilde{\boldsymbol{v}}}{\partial t} = -\tilde{\boldsymbol{v}} \cdot \nabla \tilde{\boldsymbol{v}} - \frac{1}{\rho}\nabla p + \frac{1}{\rho}\nabla \cdot \mu\left\{\nabla \tilde{\boldsymbol{v}} + (\nabla \tilde{\boldsymbol{v}})^T\right\} - \frac{2}{3\rho}\nabla \cdot \left\{\mu(\nabla \cdot \tilde{\boldsymbol{v}})\boldsymbol{I}\right\}$$
$$+ \frac{1}{\rho}\nabla \cdot \boldsymbol{S} + \frac{1}{\rho}\boldsymbol{F}_{\mathrm{s}} + \boldsymbol{g}, \tag{62}$$

where $\tilde{\boldsymbol{v}}$ is the velocity without the solid phase. Secondly, a gas–liquid–solid three phase flow is obtained by modifying the velocity in the solid phase as

$$\frac{\partial \boldsymbol{v}}{\partial t} = \frac{1}{\rho} \boldsymbol{F}_{\mathrm{p}} = \Psi \frac{\boldsymbol{v}_{\mathrm{p}} - \tilde{\boldsymbol{v}}}{\Delta t}. \tag{63}$$

Eq. (62) is solved by the simplified marker and cell (SMAC) method [58], in which the homogeneous second-derivatives in the viscous term are implicitly discretized using the Crank–Nicolson scheme and the other derivatives are explicitly discretized. An implicit discretization of the viscous term is crucial to success of a mesoscale simulation, because a small grid spacing used leads to a stringent stability condition for the viscous term. The predictor step in the SMAC method is expressed as

$$\left(1 - \frac{\Delta t}{2\rho} \nabla \cdot \mu \nabla\right) \tilde{\boldsymbol{v}}^* = \boldsymbol{v}^n + \Delta t \left[-\frac{1}{\rho} \nabla p^n - \boldsymbol{v}^n \cdot \nabla \boldsymbol{v}^n + \frac{1}{2\rho} \nabla \cdot \mu \nabla \boldsymbol{v}^n \right.$$
$$\left. + \frac{1}{\rho} \nabla \cdot \mu \left(\nabla \boldsymbol{v}^n\right)^T - \frac{2}{3\rho} \nabla \cdot \left\{ \mu (\nabla \cdot \boldsymbol{v}^n) \boldsymbol{I} \right\} + \boldsymbol{g} + \frac{1}{\rho} \nabla \cdot \boldsymbol{S} + \frac{1}{\rho} \boldsymbol{F}_{\mathrm{s}} \right], \tag{64}$$

where $\tilde{\boldsymbol{v}}^*$ is a predictive value of $\tilde{\boldsymbol{v}}$. Eq. (64) is temporally discretized using the alternative direction implicit (ADI) scheme [59], in which the tri-diagonal matrix algorithm (TDMA) [59] is employed to solve a system of equations in each direction.

In the right-hand side of Eq. (64), the advection term is discretized using the first-order upstream differencing scheme, and the pressure gradient term and the viscous term are discretized using the second-order central differencing scheme. The divergence of the stochastic stress tensor is discretized as

$$\left(\frac{1}{\rho} \nabla \cdot \boldsymbol{S}\right)_{i,j,k} = \begin{bmatrix} \frac{1}{\overline{\rho}^x_{i,j,k}} \left(\frac{S_{xx,i,j,k} - S_{xx,i-1,j,k}}{\Delta x} + \frac{S_{yx,i,j+1,k} - S_{yx,i,j,k}}{\Delta y} + \frac{S_{zx,i,j,k+1} - S_{zx,i,j,k}}{\Delta z}\right) \\ \frac{1}{\overline{\rho}^y_{i,j,k}} \left(\frac{S_{xy,i+1,j,k} - S_{xy,i,j,k}}{\Delta x} + \frac{S_{yy,i,j,k} - S_{yy,i,j-1,k}}{\Delta y} + \frac{S_{zy,i,j,k+1} - S_{zy,i,j,k}}{\Delta z}\right) \\ \frac{1}{\overline{\rho}^z_{i,j,k}} \left(\frac{S_{xz,i+1,j,k} - S_{xz,i,j,k}}{\Delta x} + \frac{S_{yz,i,j+1,k} - S_{yz,i,j,k}}{\Delta y} + \frac{S_{zz,i,j,k} - S_{zz,i,j,k-1}}{\Delta z}\right) \end{bmatrix}, \tag{65}$$

where $\overline{\rho}^x$, $\overline{\rho}^y$ and $\overline{\rho}^z$ are the densities at the cell faces normal to x, y and z direction, respectively. Based on the assumption described in Section 3.1 that a cell face is occupied by the fluid with larger density, the densities at the cell faces are expressed as

$$\overline{\rho}^x_{i,j,k} = \begin{cases} \rho_{i-1,j,k} & \bar{n}_{x,i,j,k} < 0 \\ \rho_{i,j,k} & \bar{n}_{x,i,j,k} \geq 0, \end{cases}$$
$$\overline{\rho}^y_{i,j,k} = \begin{cases} \rho_{i,j-1,k} & \bar{n}_{y,i,j,k} < 0 \\ \rho_{i,j,k} & \bar{n}_{y,i,j,k} \geq 0, \end{cases}$$
$$\overline{\rho}^z_{i,j,k} = \begin{cases} \rho_{i,j,k-1} & \bar{n}_{z,i,j,k} < 0 \\ \rho_{i,j,k} & \bar{n}_{z,i,j,k} \geq 0, \end{cases} \tag{66}$$

where

$$\bar{n}_{x,i,j,k} = \frac{n_{x,i-1,j,k} + n_{x,i,j,k}}{2},$$
$$\bar{n}_{y,i,j,k} = \frac{n_{y,i,j-1,k} + n_{y,i,j,k}}{2},$$
$$\bar{n}_{z,i,j,k} = \frac{n_{z,i,j,k-1} + n_{z,i,j,k}}{2}. \tag{67}$$

According to the statistical properties in Eq. (25), each element of the stochastic stress tensor in Eq. (65) is discretized as

$$s_{xx,i,j,k} = \sqrt{\frac{8 k_{\mathrm{B}} T \mu_{i,j,k}}{3 \Delta x \Delta y \Delta z \Delta t}} \chi_1,$$

$$s_{yy,i,j,k} = -\sqrt{\frac{2 k_{\mathrm{B}} T \mu_{i,j,k}}{3 \Delta x \Delta y \Delta z \Delta t}} \chi_1 + \sqrt{\frac{2 k_{\mathrm{B}} T \mu_{i,j,k}}{\Delta x \Delta y \Delta z \Delta t}} \chi_2,$$

$$s_{zz,i,j,k} = -\sqrt{\frac{2 k_{\mathrm{B}} T \mu_{i,j,k}}{3 \Delta x \Delta y \Delta z \Delta t}} \chi_1 - \sqrt{\frac{2 k_{\mathrm{B}} T \mu_{i,j,k}}{\Delta x \Delta y \Delta z \Delta t}} \chi_2,$$

$$s_{xy,i,j,k} = s_{yx,i,j,k} = \sqrt{\frac{2 k_{\mathrm{B}} T \overline{\mu}^{xy}_{i,j,k}}{\Delta x \Delta y \Delta z \Delta t}} \chi_3,$$

$$s_{xz,i,j,k} = s_{zx,i,j,k} = \sqrt{\frac{2k_B T \overline{\mu}_{i,j,k}^{xz}}{\Delta x \Delta y \Delta z \Delta t}} \chi_4,$$

$$s_{yz,i,j,k} = s_{zy,i,j,k} = \sqrt{\frac{2k_B T \overline{\mu}_{i,j,k}^{yz}}{\Delta x \Delta y \Delta z \Delta t}} \chi_5,$$

(68)

where χ_1, χ_2, χ_3, χ_4, χ_5 are standard normal random numbers that are mutually independent, and

$$\overline{\mu}_{i,j,k}^{xy} = \frac{1}{4}(\mu_{i-1,j-1,k} + \mu_{i,j-1,k} + \mu_{i-1,j,k} + \mu_{i,j,k}),$$

$$\overline{\mu}_{i,j,k}^{xz} = \frac{1}{4}(\mu_{i-1,j,k-1} + \mu_{i,j,k-1} + \mu_{i-1,j,k} + \mu_{i,j,k}),$$

$$\overline{\mu}_{i,j,k}^{yz} = \frac{1}{4}(\mu_{i,j-1,k-1} + \mu_{i,j,k-1} + \mu_{i,j-1,k} + \mu_{i,j,k}),$$

(69)

are the averaged viscosities at the cell edges in *xy* plane, *xz* plane and *yz* plane, respectively. The averaged viscosities are also used to discretize the cross derivatives in the viscous term. In addition, the surface tension term is discretized as

$$\left(\frac{1}{\rho}\boldsymbol{F}_s\right)_{i,j,k} = \begin{bmatrix} \frac{\sigma}{\overline{\rho}_{i,j,k}^x} \cdot \frac{\kappa_{i-1,j,k}+\kappa_{i,j,k}}{2} \cdot \frac{F_{i,j,k}-F_{i-1,j,k}}{\Delta x} \\ \frac{\sigma}{\overline{\rho}_{i,j,k}^y} \cdot \frac{\kappa_{i,j-1,k}+\kappa_{i,j,k}}{2} \cdot \frac{F_{i,j,k}-F_{i,j-1,k}}{\Delta y} \\ \frac{\sigma}{\overline{\rho}_{i,j,k}^z} \cdot \frac{\kappa_{i,j,k-1}+\kappa_{i,j,k}}{2} \cdot \frac{F_{i,j,k}-F_{i,j,k-1}}{\Delta z} \end{bmatrix}.$$

(70)

After the predictor step, we solve the Poisson equation of the corrective pressure as

$$\nabla \cdot \left(\frac{1}{\rho}\nabla p'\right) = \frac{1}{\Delta t}\left\{\nabla \cdot \tilde{\boldsymbol{v}}^* - (1-\Psi)\dot{\omega}\left|\nabla\left(\frac{1}{\rho}\right)\right|\right\},$$

(71)

where p' is the corrective pressure. The left-hand side of Eq. (71) is discretized at a cell center as

$$L_{i,j,k}^{p} = -\left(\frac{\frac{1}{\overline{\rho}_{i,j,k}^x} + \frac{1}{\overline{\rho}_{i+1,j,k}^x}}{\Delta x^2} + \frac{\frac{1}{\overline{\rho}_{i,j,k}^y} + \frac{1}{\overline{\rho}_{i,j+1,k}^y}}{\Delta y^2} + \frac{\frac{1}{\overline{\rho}_{i,j,k}^z} + \frac{1}{\overline{\rho}_{i,j,k+1}^z}}{\Delta z^2}\right)p'_{i,j,k}$$

$$+ \frac{1}{\Delta x^2 \overline{\rho}_{i,j,k}^x}p'_{i-1,j,k} + \frac{1}{\Delta x^2 \overline{\rho}_{i+1,j,k}^x}p'_{i+1,j,k} + \frac{1}{\Delta y^2 \overline{\rho}_{i,j,k}^y}p'_{i,j-1,k}$$

$$+ \frac{1}{\Delta y^2 \overline{\rho}_{i,j+1,k}^y}p'_{i,j+1,k} + \frac{1}{\Delta z^2 \overline{\rho}_{i,j,k}^z}p'_{i,j,k-1} + \frac{1}{\Delta z^2 \overline{\rho}_{i,j,k+1}^z}p'_{i,j,k+1}.$$

(72)

The right-hand side of Eq. (71) is discretized at a cell center as

$$R_{i,j,k}^{p} = \frac{1}{\Delta t}\left\{\frac{\tilde{u}_{i+1,j,k}^* - \tilde{u}_{i,j,k}^*}{\Delta x} + \frac{\tilde{v}_{i,j+1,k}^* - \tilde{v}_{i,j,k}^*}{\Delta y} + \frac{\tilde{w}_{i,j,k+1}^* - \tilde{w}_{i,j,k}^*}{\Delta z} - (1-\Psi_{i,j,k})\dot{\omega}\right.$$

$$\left.\times \sqrt{\frac{\left(\frac{1}{\overline{\rho}_{i+1,j,k}^x} - \frac{1}{\overline{\rho}_{i,j,k}^x}\right)^2}{\Delta x^2} + \frac{\left(\frac{1}{\overline{\rho}_{i,j+1,k}^y} - \frac{1}{\overline{\rho}_{i,j,k}^y}\right)^2}{\Delta y^2} + \frac{\left(\frac{1}{\overline{\rho}_{i,j,k+1}^z} - \frac{1}{\overline{\rho}_{i,j,k}^z}\right)^2}{\Delta z^2}}\right\},$$

(73)

where $\tilde{u}^*$, $\tilde{v}^*$, $\tilde{w}^*$ are the components of $\tilde{\boldsymbol{v}}^*$. The converged solution of $L_{i,j,k}^{p} = R_{i,j,k}^{p}$ is obtained by a line relaxation method, in which the tri-diagonal matrix algorithm (TDMA) is adopted to solve a system of equations in each line. The convergence criteria is given by

$$\sqrt{\frac{\sum_{i,j,k}(L_{i,j,k}^{p} - R_{i,j,k}^{p})^2}{\sum_{i,j,k}R_{i,j,k}^{p}{}^2}} \leq 10^{-3}.$$

(74)

Using the corrective pressure, the pressure and the velocity without the solid phase are obtained in the corrector step as

$$p = p^n + p',$$

(75)

$$\tilde{\boldsymbol{v}} = \tilde{\boldsymbol{v}}^* - \frac{\Delta t}{\rho}\nabla p'.$$

(76)

Finally, the velocity of the gas–liquid–solid three phase flow is obtained by discretizing Eq. (63) as

$$u_{i,j,k}^{n+1} = \tilde{u}_{i,j,k} - \frac{\Psi_{i-1,j,k} + \Psi_{i,j,k}}{2}\left(\frac{u_{\mathrm{p},i-1,j,k} + u_{\mathrm{p},i,j,k}}{2} - \tilde{u}_{i,j,k}\right),$$

$$v_{i,j,k}^{n+1} = \tilde{v}_{i,j,k} - \frac{\Psi_{i,j-1,k} + \Psi_{i,j,k}}{2}\left(\frac{v_{\mathrm{p},i,j-1,k} + v_{\mathrm{p},i,j,k}}{2} - \tilde{v}_{i,j,k}\right),$$

$$w_{i,j,k}^{n+1} = \tilde{w}_{i,j,k} - \frac{\Psi_{i,j,k-1} + \Psi_{i,j,k}}{2}\left(\frac{w_{\mathrm{p},i,j,k-1} + w_{\mathrm{p},i,j,k}}{2} - \tilde{w}_{i,j,k}\right), \tag{77}$$

where $\tilde{u}$, $\tilde{v}$, $\tilde{w}$ are the components of $\tilde{\boldsymbol{v}}$ and u_{p}, v_{p}, w_{p} are the components of $\boldsymbol{v}_{\mathrm{p}}$.

For a numerical stability, there are time step constraints for the transport terms in Eq. (62). If a temporally first-order scheme is adopted, the Courant–Friedrichs–Levy (CFL) stability condition for the advection term is expressed as

$$\max\left(\frac{|\overline{u}_{i,j,k}|}{\Delta x} + \frac{|\overline{v}_{i,j,k}|}{\Delta y} + \frac{|\overline{w}_{i,j,k}|}{\Delta z}\right)\Delta t \leq 1. \tag{78}$$

The stability condition for the viscous term is expressed as [60]

$$\max\left(\frac{\mu_{\mathrm{l}}}{\rho_{\mathrm{l}}}, \frac{\mu_{\mathrm{g}}}{\rho_{\mathrm{g}}}\right)\left(\frac{1}{\Delta x^2} + \frac{1}{\Delta y^2} + \frac{1}{\Delta z^2}\right)\Delta t \leq \frac{1}{2}. \tag{79}$$

The stability condition for the surface force term is expressed as [40]

$$\sqrt{\frac{\pi\sigma}{\rho_{\mathrm{l}} + \rho_{\mathrm{g}}}}\left(\frac{1}{\Delta x^{3/2}} + \frac{1}{\Delta y^{3/2}} + \frac{1}{\Delta z^{3/2}}\right)\Delta t \leq \frac{1}{2}. \tag{80}$$

The present simulation is hardly restricted by the stability conditions of Eqs. (78) and (79), because the flow speed is much small and the viscous term is treated implicitly. In fact, the implicit treatment of the homogeneous second-derivatives in Eq. (64) allows us to adopt a time step five times more than the time step that is specified in Eq. (79). Consequently, the computational time step is commonly constrained by the stability condition of Eq. (80).

In the present simulation method, the substrate is treated as a still solid phase and put on the bottom boundary of a cuboidal computational domain. Then the bottom boundary is located in the solid phase, in which p is given by a zeroth order extrapolation, ϕ is given by a first-order extrapolation, and $u = v = w = s_{xz} = s_{zx} = s_{yz} = s_{zy} = 0$. On the top boundary, a flow out boundary condition is imposed, in which ϕ, u, v are given by a first-order extrapolation, w is given by applying the condition of zero divergence, s_{zx}, s_{zy} are given by a zeroth order extrapolation, p is fixed to the atmospheric pressure p_∞ and $s_{xx} = s_{yy} = s_{zz} = s_{xy} = s_{yx} = 0$. In addition, a periodic boundary condition is imposed on the side boundaries.

3.4. Solving particle motion: dual time stepping and periodic boundary

The forces and the torques exerted on a colloidal particle have different characteristic times. The characteristic times of $\boldsymbol{F}_{\mathrm{c}}$, $\boldsymbol{F}_{\mathrm{e}}$, $\boldsymbol{F}_{\mathrm{v}}$ in Eq. (34) and $\boldsymbol{T}_{\mathrm{c}}$ in Eq. (35) are associated with the motion of molecules. The characteristic times of $\boldsymbol{F}_{\mathrm{h}}$ in Eq. (34) and $\boldsymbol{T}_{\mathrm{h}}$ in Eq. (35), on the other hand, are associated with the motion of colloidal particles. The former characteristic times are typically smaller than the latter ones. The present simulation method is able to separate the time evolution of particle motion from the time evolution of flow, because both time evolutions are weakly coupled with each other. Therefore, in addition to Δt for evaluating $\boldsymbol{F}_{\mathrm{h}}$ and $\boldsymbol{T}_{\mathrm{h}}$, a smaller time step $\Delta t'$ is used to evaluate $\boldsymbol{F}_{\mathrm{c}}$, $\boldsymbol{F}_{\mathrm{e}}$, $\boldsymbol{F}_{\mathrm{v}}$, $\boldsymbol{T}_{\mathrm{c}}$. This dual time stepping, which has been proposed in our previous work [26], saves the computational cost considerably, because the evaluation of $\boldsymbol{F}_{\mathrm{h}}$ and $\boldsymbol{T}_{\mathrm{h}}$ requires rather expensive computation of the flow. The relation of $\Delta t'$ and Δt is given by

$$\Delta t = \lambda \Delta t', \tag{81}$$

where λ is a positive integer. In a word, the flow and the particle motion are evolved with Δt and $\Delta t'$, respectively.

Eqs. (34) and (35) are temporally discretized using the first-order Euler explicit scheme as

$$\boldsymbol{V}_l^{m+1} = \boldsymbol{V}_l^m + \frac{\Delta t'}{M}\left(\boldsymbol{F}_{\mathrm{c},l}^m + \boldsymbol{F}_{\mathrm{e},l}^m + \boldsymbol{F}_{\mathrm{v},l}^m + \boldsymbol{F}_{\mathrm{h},l}^n\right), \tag{82}$$

$$\boldsymbol{\Omega}_l^{m+1} = \boldsymbol{\Omega}_l^m + \frac{\Delta t'}{I}\left(\boldsymbol{T}_{\mathrm{c},l}^m + \boldsymbol{T}_{\mathrm{h},l}^n\right), \tag{83}$$

and Eq. (36) is temporally discretized using the first-order Euler implicit scheme as

$$\boldsymbol{X}_l^{m+1} = \boldsymbol{X}_l^m + \Delta t' \boldsymbol{V}_l^{m+1}, \tag{84}$$

where m is index for temporal discretization for the particle motion. At each time step of the flow computation, initializations are performed as $\boldsymbol{V}_l^{m=0} = \boldsymbol{V}_l^n$, $\boldsymbol{\Omega}_l^{m=0} = \boldsymbol{\Omega}_l^n$, $\boldsymbol{X}_l^{m=0} = \boldsymbol{X}_l^n$. After repeating the time evolution of Eqs. (82), (83) and (84) λ times, the solution of the particle motion at the next time step is obtained as $\boldsymbol{V}_l^{n+1} = \boldsymbol{V}_l^{m=\lambda}$, $\boldsymbol{\Omega}_l^{n+1} = \boldsymbol{\Omega}_l^{m=\lambda}$, $\boldsymbol{X}_l^{n+1} = \boldsymbol{X}_l^{m=\lambda}$. Note that $\boldsymbol{F}_{\mathrm{h},l}^n$ and $\boldsymbol{T}_{\mathrm{h},l}^n$ remain constant during the repeat.
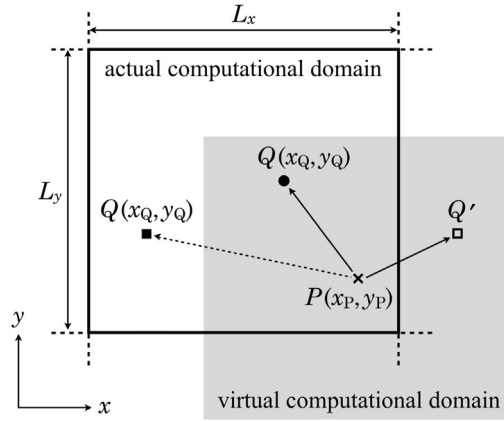
Fig. 8. A schematic picture of measuring distance from the particle P to the particle Q. The light gray rectangle represents the virtual computational domain centering around P. The distance to the particle Q ($\bullet$) in the virtual computational domain is directly measured. The distance to the imaginary particle Q' ($\square$) is substituted for the distance to the particle Q ($\blacksquare$) outside the virtual computational domain.

The components of $\boldsymbol{F}_{\mathrm{h},l}$ are discretized at cell centers as

$$F_{\mathrm{h},l,x} = -\sum_{i,j,k}\big\{F_{\mathrm{p},x,i,j,k} - \Psi_{i,j,k}(\rho_{\mathrm{p}} - \rho_{i,j,k})g_x\big\}\Delta x\Delta y\Delta z,$$

$$F_{\mathrm{h},l,y} = -\sum_{i,j,k}\big\{F_{\mathrm{p},y,i,j,k} - \Psi_{i,j,k}(\rho_{\mathrm{p}} - \rho_{i,j,k})g_y\big\}\Delta x\Delta y\Delta z,$$

$$F_{\mathrm{h},l,z} = -\sum_{i,j,k}\big\{F_{\mathrm{p},z,i,j,k} - \Psi_{i,j,k}(\rho_{\mathrm{p}} - \rho_{i,j,k})g_z\big\}\Delta x\Delta y\Delta z, \tag{85}$$

where g_x, g_y, g_z are the components of $\boldsymbol{g}$ and $F_{\mathrm{p},x}$, $F_{\mathrm{p},y}$, $F_{\mathrm{p},z}$ are the components of $\boldsymbol{F}_{\mathrm{p}}$ estimated at cell centers as

$$F_{\mathrm{p},x,i,j,k} = \Psi_{i,j,k}\rho_{i,j,k}\frac{u_{\mathrm{p},i,j,k} - \overline{u}_{i,j,k}}{\Delta t},$$

$$F_{\mathrm{p},y,i,j,k} = \Psi_{i,j,k}\rho_{i,j,k}\frac{v_{\mathrm{p},i,j,k} - \overline{v}_{i,j,k}}{\Delta t},$$

$$F_{\mathrm{p},z,i,j,k} = \Psi_{i,j,k}\rho_{i,j,k}\frac{w_{\mathrm{p},i,j,k} - \overline{w}_{i,j,k}}{\Delta t}. \tag{86}$$

The components of $\boldsymbol{T}_{\mathrm{h},l}$ are discretized at cell centers as

$$T_{\mathrm{h},l,x} = -\sum_{i,j,k}(\bar{r}_{l,y,i,j,k}F_{\mathrm{p},z,i,j,k} - \bar{r}_{l,z,i,j,k}F_{\mathrm{p},y,i,j,k})\Delta x\Delta y\Delta z,$$

$$T_{\mathrm{h},l,y} = -\sum_{i,j,k}(\bar{r}_{l,z,i,j,k}F_{\mathrm{p},x,i,j,k} - \bar{r}_{l,x,i,j,k}F_{\mathrm{p},z,i,j,k})\Delta x\Delta y\Delta z,$$

$$T_{\mathrm{h},l,z} = -\sum_{i,j,k}(\bar{r}_{l,x,i,j,k}F_{\mathrm{p},y,i,j,k} - \bar{r}_{l,y,i,j,k}F_{\mathrm{p},x,i,j,k})\Delta x\Delta y\Delta z, \tag{87}$$

where $\bar{r}_{l,x}$, $\bar{r}_{l,y}$, $\bar{r}_{l,z}$ are the components of $\bar{\boldsymbol{r}}_l$. Note that the summations in Eqs. (85) and (87) are performed in the l-th particle domain.

We need to measure the distance between particles to evaluate $\boldsymbol{F}_{\mathrm{c}}$, $\boldsymbol{F}_{\mathrm{e}}$, $\boldsymbol{F}_{\mathrm{v}}$ and $\boldsymbol{T}_{\mathrm{c}}$. The measurement is performed for not only the particles in the computational domain but also the particles outside the domain, because the periodic condition is imposed on the side boundaries of the computational domain. Fig. 8 shows a schematic picture of measuring distance from the particle $P(x_{\mathrm{p}}, y_{\mathrm{p}})$ to the particle $Q(x_{\mathrm{Q}}, y_{\mathrm{Q}})$. We consider the virtual computational domain centering around P, whose size is equal to the actual computational domain. If Q is in the virtual computational domain, the distance to Q is measured. If Q is, on the other hand, outside the virtual computational domain, the distance to the imaginary particle Q' is measured. Consequently, the distance from P to Q is expressed as

$$R = \sqrt{R_x{}^2 + R_y{}^2}, \tag{88}$$

where

(a) conventional way (b) present way
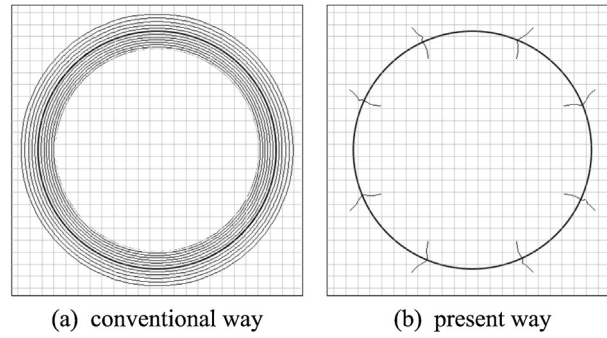
Fig. 9. Estimated curvature field at the cross section of the droplet for $d/h = 20$, where iso-curvature contours are depicted only in the region of free surface using: (a) the conventional way; (b) the present way. The interval of each contour line is $0.025\kappa_{exact}$, where $\kappa_{exact} = 4/d$ is the exact curvature of the sharp interface between gas and liquid that is depicted as the thick circle.

$$R_x = x_Q - x_P - L_x \, \text{int}\left(\frac{x_Q - x_P}{L_x/2}\right),$$

$$R_y = y_Q - y_P - L_y \, \text{int}\left(\frac{y_Q - y_P}{L_y/2}\right). \tag{89}$$

Here L_x and L_y are the side lengths of the computational domain in x and y direction, respectively.

4. Simulation results

We illustrate some simulation results to demonstrate the capability of the present simulation method. Firstly, two important components in the present method, such as the way of curvature estimation and the IFS model, are demonstrated in the following subsections. Then simulations of drying colloidal suspension on a substrate are performed. We treat the flow field as follows: $\rho_l = 10^3$ kg/m^3, $\rho_g = 1$ kg/m^3, $\mu_l = 10^{-3}$ Ns/m^3, $\mu_g = 2 \times 10^{-5}$ Ns/m^3, $\sigma = 0.073$ N/m, $T = 300$ K, $p_\infty = 10^5$ N/m^2 and $|\mathbf{g}| = 9.8$ m/s^2. The spherical particles have the same diameter of $d_p = 10^{-6}$ m and the same density of $\rho_p = 2 \times 10^3$ kg/m^3. The Young's modulus and the Poisson's ratio of the spherical particles and the substrate are 10^9 N/m^2 and 0.3, respectively.

4.1. Simulation of a still droplet without drying

A simulation of a still droplet with the diameter of $d = 5 \times 10^{-4}$ m without drying is performed as a demonstration of the present way of curvature estimation including the virtual grid differencing. Both the stochastic stress term and the gravitational acceleration term in the hydrodynamic equations are neglected to emphasize a spurious flow induced by the simulation. The simulation is performed on two grid resolutions of $d/h = 10$ and 20 to investigate the grid dependency of the way of curvature estimation. The initial condition is $\mathbf{v} = 0$ and $p = p_\infty$ in a whole computational domain. The simulation time is $t = 10t_d$, where $t_d = 0.25\pi\sqrt{\rho_l d^3/\sigma}$ is the theoretical oscillation period of an inviscid droplet [61]. The converged solution has been obtained at $t = 10t_d$. Fig. 9 shows the estimated curvature field at the cross section of the droplet for $d/h = 20$. A cell-centered curvature is estimated by the conventional way as well as the present way. When we use the conventional way, the curvature is directly obtained from the surrounding level set functions using Eq. (27). As shown in Fig. 9(a), the curvature field has a concentric distribution in the region of free surface, because the curvature is a function of the local level set function. In other words, the estimated curvature decreases outward in a radial direction. On the other hand, the curvature remains nearly constant in the region of free surface when we use the present way, as shown in Fig. 9(b). This is because all the curvatures in the region of free surface is calculated on the sharp interface between gas and liquid.

Fig. 10 shows the computed velocity field at the cross section of the droplet at $t = 10t_d$. Figs. 10(a) and (b) represent the spurious flow induced by the conventional way of curvature estimation and the present way of curvature estimation, respectively. As shown in Fig. 10(a), the conventional way induces a large spurious flow that is severely affected by the computational grid. Namely, main outward spurious flow emanates from the free surface along the grid lines. As shown in Fig. 10(b), on the other hand, the present way induces a much smaller spurious flow than the conventional way, in which the induced spurious flow is almost independent of the direction of the computational grid. In addition, the spurious flow induced by the conventional way depends strongly on the grid resolution, whereas the spurious flow induced by the present way is insensitive to the grid resolution.

Fig. 11 shows the computational results of the magnitude of spurious flow and the error of the Laplace pressure as a function of grid resolution. The magnitude of the spurious flow is represented by the dimensionless number $Ca = \mu_l \bar{v}/\sigma$, where $\bar{v}$ is the root mean square of velocity in the computational domain. The error of the Laplace pressure is represented by the dimensionless value $\Delta p' = |\Delta p - \Delta p_{exact}|/\Delta p_{exact}$, where Δp is the computed Laplace pressure and $\Delta p_{exact} = 4\sigma/d$

$d/h = 10$ $d/h = 20$

(a) conventional way

$d/h = 10$ $d/h = 20$
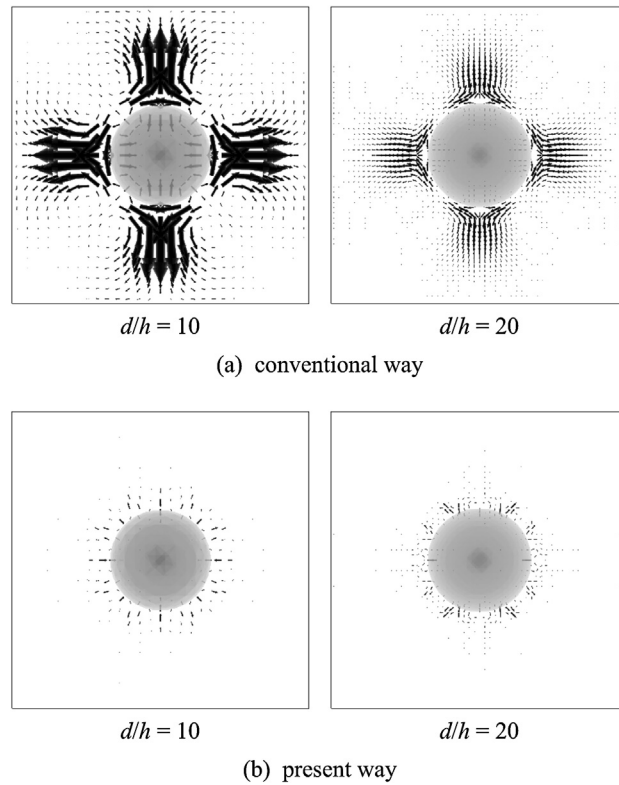
(b) present way

Fig. 10. Computed velocity field at the cross section of the droplet at $t = 10t_d$ using the curvature estimated by: (a) the conventional way; (b) the present way. The scale of velocity vectors is the same in every case.
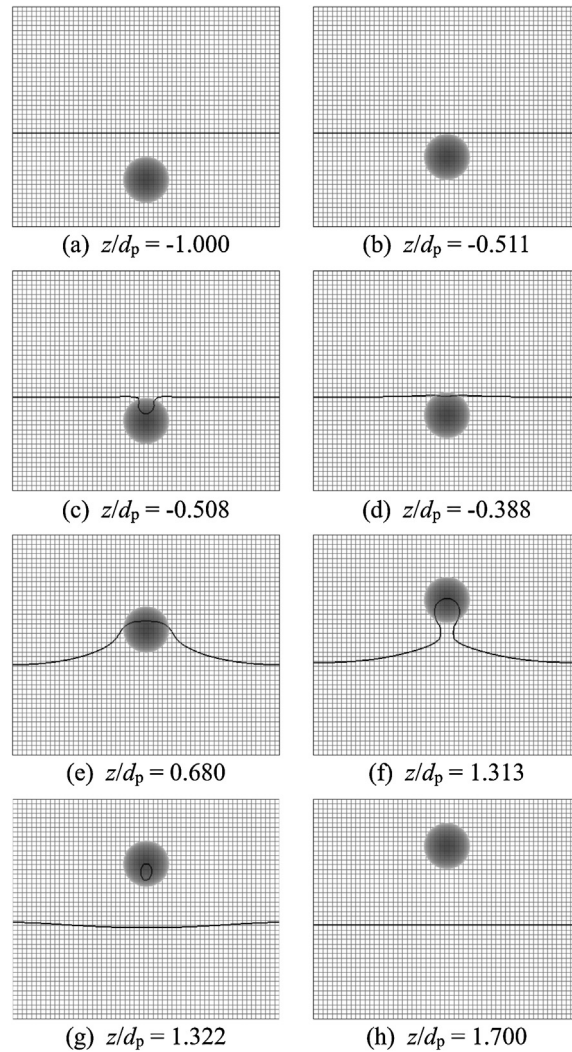

(a) magnitude of spurious flow   (b) error of Laplace pressure
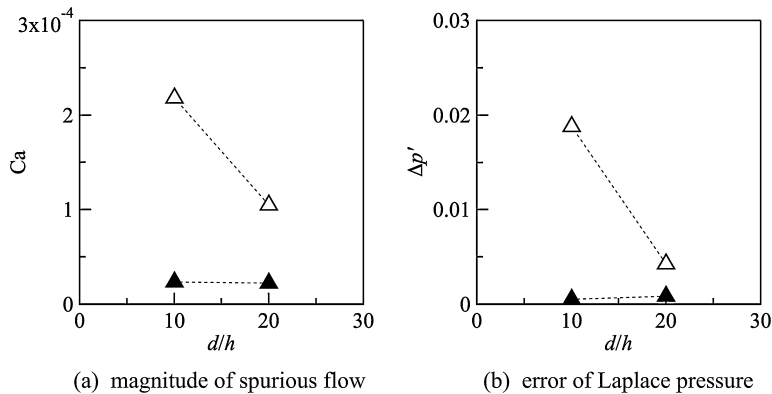
Fig. 11. Computational results of: (a) the magnitude of spurious flow; (b) the error of the Laplace pressure as a function of grid resolution. The results obtained by the present way and those obtained by the conventional way are depicted as the solid triangles (▲) and the open triangles (△), respectively.

is the exact Laplace pressure. The Laplace pressure is computed using a volume average of the pressure in the droplet. As shown in Fig. 11(a), a mean speed of the spurious flow obtained by the present way is about an order of magnitude less than that obtained by the conventional way. As shown in Fig. 11(b), the error of the Laplace pressure induced by the present way is a fraction of that induced by the conventional way. Furthermore, the present way of curvature estimation is insensitive to the grid resolution and has a good performance even on a coarse grid unlike the conventional way. In other words, the present way is able to estimate accurately the curvature of a smaller droplet compared with the conventional way. It is noted that the additional computational cost of the present way over the conventional way is negligible small.

4.2. Simulation of a sphere moving across a free surface without drying

A simulation of a sphere moving across a free surface without drying is performed as a demonstration of the IFS model. The sphere initially located in the liquid phase is forced to move toward the gas phase at the constant speed of $v_z =$

(a) $z/d_p = -1.000$

(b) $z/d_p = -0.511$

(c) $z/d_p = -0.508$

(d) $z/d_p = -0.388$

(e) $z/d_p = 0.680$

(f) $z/d_p = 1.313$

(g) $z/d_p = 1.322$

(h) $z/d_p = 1.700$

Fig. 12. Snapshots of the sphere and the gas–liquid interface at the cross section of the sphere for $d_p/h = 10$. Both the free surface and the virtual free surface are depicted as the contour line of $\phi = 0$. The position of the spherical center z (positive in upward direction) is measured from the initial free surface. Note that the top of the sphere coincides geometrically with the initial free surface when $z/d_p = -0.5$.

0.05 m/s. In other words, the motion equations of the sphere are not solved. The stochastic stress term in the hydrodynamic equations is neglected. The specified contact angle on the sphere is 30 degrees. The simulation is performed on two grid resolutions of $d_p/h = 5$ and 10 to investigate the grid dependency of the IFS model. Fig. 12(a) shows the initial snapshot of the sphere and the free surface for $d_p/h = 10$, in which the spherical center z is located at d_p below the flat free surface. Fig. 12(b) shows the snapshot just before the contact between the top of the sphere and the free surface, in which the free surface remains flat. Fig. 12(c) shows the snapshot just after the contact, in which the virtual free surface in the sphere curves convex downward. By way of the IFS model, the curved virtual free surface exerts a upward hydrodynamic force on the sphere, which means a vertical capillary force. The contact between the sphere and the free surface takes place at less than $z/d_p = -0.5$, because the free surface has a finite thickness. As the sphere goes up, the virtual free surface flattens at a certain moment, as shown in Fig. 12(d). The vertical capillary force is not exerted on the sphere at that time. As the sphere goes up further, then the virtual free surface curves convex upward, so that the vertical capillary force is exerted downward on the sphere. Fig. 12(e) shows the snapshot when the contact line coincides with the horizontal great circle of the sphere. Fig. 12(f) shows the snapshot just before a breakup of the free surface, in which a necking of the free surface takes place. Fig. 12(g) shows the snapshot just after the breakup of the free surface, in which a broken virtual free surface remains in the sphere. The broken virtual free surface does not exert the capillary force on the sphere, because it forms a closed surface. As shown in Fig. 12(h), the spherical center reaches finally at $z = 1.7d_p$, and the free surface becomes flattened again. It is noted that the free surface intersects with the spherical surface at the specified contact angle in Figs. 12(c), (d), (e) and (f).
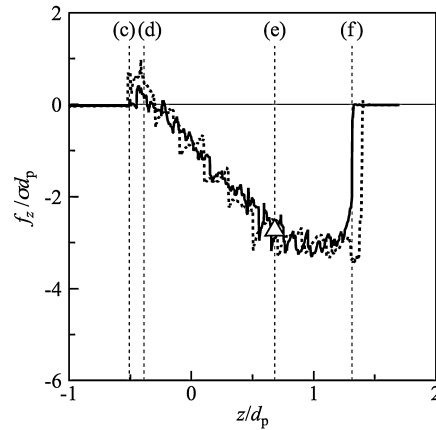
Fig. 13. Vertical hydrodynamic forces exerted on the sphere (positive in upward direction) as a function of the position of the spherical center. The computational results for $d_p/h = 5$ and 10 are depicted as the dotted curve and the solid curve, respectively. The positions (c)–(f) in the figure correspond to Figs. 12(c)–(f), respectively. The analytical vertical capillary force exerted on a still sphere is depicted as the open triangle ($\triangle$).

We performed a quantitative validation of the IFS model in Ref. [38], in which a computed vertical capillary force exerted on a still sphere protruding a free surface has been agreed well with an analytical formula. Here we illustrate a capillary force exerted on the mobile sphere shown in Fig. 12. Fig. 13 shows the dimensionless vertical hydrodynamic forces as a function of the position of the spherical center. Although the hydrodynamic force includes a viscous drag, the viscous drag is negligible small compared with the capillary force in this case. Therefore, the axis of ordinate in the figure represents, in effect, the vertical capillary force exerted on the sphere. The capillary force is naturally exerted when the free surface intersects with the sphere, namely, from the position (c) to (f). From the position (c) to (d), the capillary force is exerted in upward direction. On the other hand, the capillary force is exerted in downward direction from the position (d) to (f). This reverse of the capillary force is due to the shape change of the virtual free surface in the sphere, as described in Fig. 12. When the contact line coincides with the horizontal great circle of the sphere at the position (e), the vertical capillary force exerted on a still sphere with the contact angle of 30 degrees is analytically obtained as $f_z = 0.5\sqrt{3}\pi\sigma d_p$. The computational result for the mobile sphere agrees quite well with the analytical solution for a still sphere. Since the magnitude of the downward force is larger than that of the upward force and the distance for which the downward force acts are larger than that for which the upward force acts, a work is required to pull up the sphere from the liquid phase to the gas phase. This corresponds to that the sphere is hydrophilic. The vertical capillary force in Fig. 13 oscillates with higher frequency than the motion of the sphere. This may be due to a discretization error in computing the surface tension exerted on the virtual free surface. Due to a lack of grid resolution, the amplitude of the oscillation for $d_p/h = 5$ is larger than that for $d_p/h = 10$ and the breakup of the free surface for $d_p/h = 5$ gets behind that for $d_p/h = 10$. Nevertheless, the computed vertical capillary force agrees well with the analytical solution even for $d_p/h = 5$. It can be said that the IFS model enables us to estimate accurately the vertical capillary force exerted on a sphere even for the grid resolution of $d_p/h = 5$.

Fig. 14 shows the volumetric error of liquid phase as a function of the position of the spherical center. The volume of liquid slightly increases during a period in which the sphere moves across the free surface. This may be due to a discretization error in computing the area of free surface by Eq. (13) and the volume of liquid by Eq. (15). On the other hand, the volume of liquid is completely conserved if the free surface moves without protrusion of the sphere. In addition, the volumetric error of liquid phase is insensitive to the grid resolution, as shown in Fig. 14. Although the volumetric error of liquid phase should be fixed for more precise simulations, the present error can be within an acceptable level.
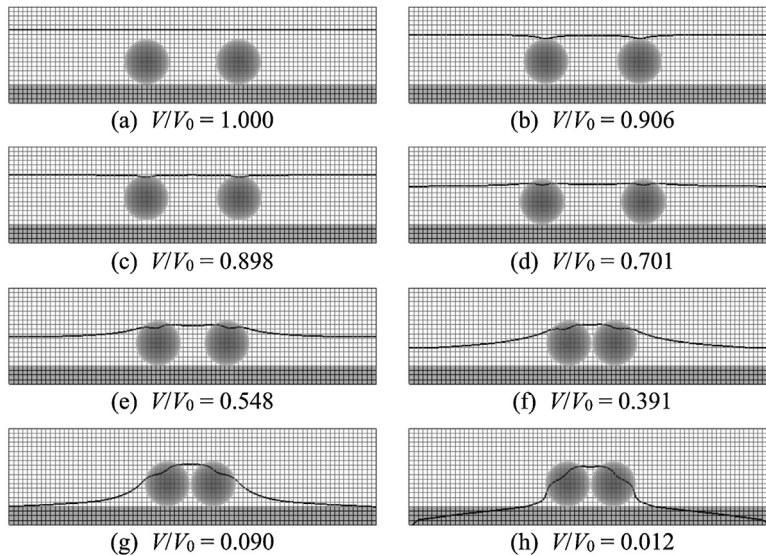
4.3. Simulation of two spheres moving along a free surface with drying

A simulation of two spheres moving along a free surface with drying is performed as a demonstration of the IFS model. The spheres are initially immersed in a liquid film on a substrate. Then the liquid film dries with $\dot{\omega} = 10$ kg/m^2 s, so that the spheres protrude from the free surface. The vaporization mass flow rate may be rather larger than that in an actual system. A large mass flow rate leads to a large velocity jump across the free surface when the density ratio between gas phase and liquid phase is high. In fact, the velocity jump is up to about 10 m/s in the present simulation. Such a large velocity jump has possible numerical instabilities. We have adopted this mass flow rate to illustrate the robustness of the present method. Naturally, the present method is applicable to a phase change flow with a smaller mass flow rate.

In the simulation, the spheres have two degrees of freedom of motion, such as translational motion without rotation in the cross sectional plane of the spheres. To emphasize the capillary force obtained by the IFS model, the stochastic stress term in the hydrodynamic equations is neglected. We also ignore the electrostatic force, the van der Waals force and the tangential contact force that are exerted on the spheres. In a word, each sphere moves under the hydrodynamic force and the normal contact force that are exerted by another sphere and the substrate. The specified contact angle on the sphere
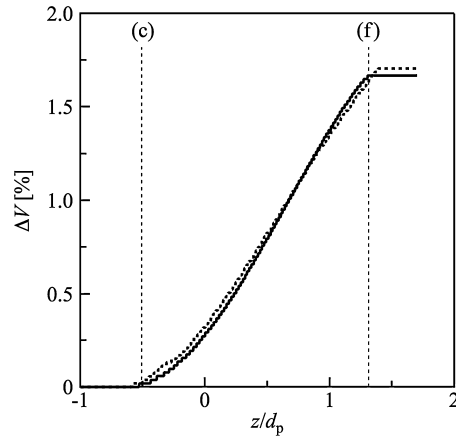
Fig. 14. Volumetric error of liquid phase $\Delta V = (V/V_0 - 1) \times 100$ as a function of the position of the spherical center, where V is the computed volume of liquid phase and V_0 is the initial volume of liquid phase. The computational results for $d_p/h = 5$ and 10 are depicted as the dotted curve and the solid curve, respectively. The positions (c) and (f) in the figure correspond to Fig. 12(c) and (f), respectively.


(a) $V/V_0 = 1.000$

(b) $V/V_0 = 0.906$

(c) $V/V_0 = 0.898$

(d) $V/V_0 = 0.701$

(e) $V/V_0 = 0.548$

(f) $V/V_0 = 0.391$

(g) $V/V_0 = 0.090$

(h) $V/V_0 = 0.012$

Fig. 15. Snapshots of the spheres and the gas–liquid interface at the cross section of the spheres for $d_p/h = 10$. Both the free surface and the virtual free surface in the spheres are depicted as the contour line of $\phi = 0$. The gray rectangle in each snapshot is the substrate imposed in the computational domain. The volume of liquid phase V is normalized by the initial volume of liquid phase V_0.

and that on the substrate are 30 degrees and 0 degrees, respectively. The simulation is performed on three grid resolutions of $d_p/h = 5$, 10 and 15 to investigate the grid dependency of the IFS model.

Fig. 15(a) shows the initial snapshot of the spheres and the free surface for $d_p/h = 10$, in which the spheres are attached on the substrate. As the free surface goes down due to the drying, the free surface is in contact with the top of the spheres, in which the virtual free surface in the spheres curves convex downward, as shown in Fig. 15(b). The curved virtual free surface exerts upward capillary forces on the spheres, so that the spheres are floated from the substrate, as shown in Fig. 15(c). During the flotation of the spheres, the virtual free surface is almost flat and capillary forces do not act on the spheres. In fact, the vertical capillary force exerted on a floating body on a free surface is balanced with the gravitational force exerted on the body. Therefore, the "flotation capillary force" exerted on a colloidal particle whose diameter is less than 10 μm is negligible small [2]. As the free surface further goes down, the spheres are re-attached on the substrate, as shown in Fig. 15(d). From this point forward, menisci are formed on both sides of the spheres. The menisci become asymmetric on both sides of each sphere, because the menisci between the spheres are overlapped each other. The asymmetric menisci lead to an imbalance of surface tensions exerted on the contact lines. As a result, an attractive force is exerted on the spheres and the spheres approach each other, as shown in Fig. 15(e). The attractive force exerted between the spheres is called "immersion capillary force" [2]. The immersion capillary force is effective even for single nano-sized particles unlike the flotation capillary force, because the immersion capillary force does not need to balance with the gravitational force. Then the spheres are in contact with each other, as shown in Fig. 15(f). From this point forward, the drying of liquid phase takes
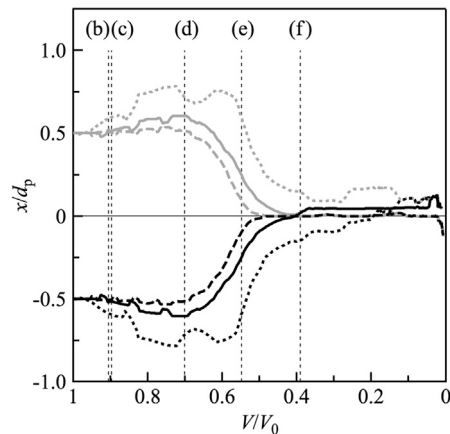
Fig. 16. Positions of the closest points of two spheres as a function of the volume of liquid phase. The black curves and the gray curves represent the first sphere and the second sphere, respectively. The computational results for $d_p/h = 5, 10$ and 15 are depicted as the dotted curve, the solid curve and the dashed curve, respectively. The volumes (b)–(f) in the figure correspond to Figs. 15(b)–(f), respectively.
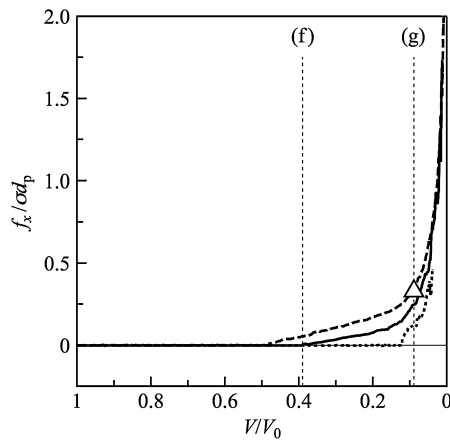
Fig. 17. Lateral hydrodynamic force exerted on the first sphere as a function of the volume of liquid phase. The computational results for $d_p/h = 5, 10$ and 15 are depicted as the dotted curve, the solid curve and the dashed curve, respectively. The approximate analytical solution of the lateral immersion capillary force is depicted as the open triangle ($\triangle$). The volumes (f) and (g) in the figure correspond to Figs. 15(f) and (g), respectively.

place mainly outside the aggregated spheres. Fig. 15(g) shows the snapshot just before the free surface is in contact with the substrate. In other words, dewetting starts from this point. Eventually, the volume of liquid phase in the computational domain approaches zero, as shown in Fig. 15(h).

Fig. 16 shows the positions of the closest points of two spheres as a function of the volume of liquid phase. The distance between the closest points is d_p at first, as shown in Fig. 16. For $d_p/h = 15$, two spheres hardly move in x direction during the flotation of the spheres from the substrate. After the reattachment of the spheres on the substrate, the distance between the closest points rapidly decreases because an attractive immersion capillary force is exerted on the spheres. Eventually, two spheres are in contact with each other at the midpoint between the initial positions. For $d_p/h = 10$, the distance between the closest points slightly increases during the flotation of the spheres, although the motion of the spheres is roughly the same as that for $d_p/h = 15$. The increase of the distance between the closest points is more significant for $d_p/h = 5$. Due to the significant increase of the distance during the flotation of the spheres, the contact of two spheres gets considerably behind those for $d_p/h = 15$ and 10. It can be said that the grid resolution of $d_p/h = 5$ is insufficient to simulate two spheres moving along the free surface.

Fig. 17 shows the lateral hydrodynamic force exerted on the first sphere as a function of the volume of liquid phase. The lateral hydrodynamic force is close to zero when the spheres are in motion, because an immersion capillary force balances with a viscous drag force. The lateral hydrodynamic force increases after the spheres are in contact with each other, because the viscous drag becomes zero. Furthermore, the lateral hydrodynamic force increases, because the immersion capillary force increases with increasing asymmetricity of the menisci on both sides of each sphere. An approximate analytical form of the lateral immersion capillary force exerted on two identical spheres is given as $f_x = 2\pi\sigma r_c^2 \sin^2\beta/L$, where r_c is the radius of the contact circle on the spheres, β is the slope angle and L is the distance between the spherical centers [2]. Note that β means the angle between a horizontal line and the menisci outside the spheres. Under the present periodic

boundary condition, the approximate analytical form is modified as $f_x = 2\pi\sigma r_c^2 \sin^2\beta\{1/L - 1/(L_x - L)\}$, where L_x is the length of the computational domain in x direction. The approximate analytical solution of the lateral immersion capillary force is shown in Fig. 17, where r_c and β are read from Fig. 15(g). As shown in Fig. 17, the computational result for $d_p/h = 15$ agrees quite well with the approximate analytical solution. On the other hand, the computational results are underestimated for $d_p/h = 10$ and 5. Therefore, it is preferable to use the grid resolution of $d_p/h = 15$ to estimate precisely the lateral immersion capillary force when two spheres are in contact. It is noted that the IFS model using the grid resolution of $d_p/h = 10$ enables us to estimate accurately the lateral immersion capillary force when two spheres have a distance from each other [38].

4.4. Simulations of drying colloidal suspension on a substrate

Simulations of drying colloidal suspension on a substrate are performed as a demonstration of the present method. We assume a thin liquid film on a substrate containing identical 130 spherical particles that dries with $\dot\omega = 10$ kg/m^2 s. The size of the substrate is $15d_p \times 15d_p$, so that the coverage ratio to the close-packed particles is 0.5. The particles have six degrees of freedom of motion. The particles are subject to all the forces modeled in Section 2 except the electrostatic force, such as the stochastic force, the tangential contact force and the van der Waals force of particle-to-particle and particle-to-substrate. The Hamaker constant of the particles and the substrate used to estimate the van der Waals force is 10^{-20} J. The frictional coefficient of particle-to-particle and particle-to-substrate is 0.1. Both the hydrophilic particles with the contact angle of $\theta = 30°$ and the hydrophobic particles with the contact angle of $\theta = 120°$ are simulated. The contact angle on the substrate is 0 degrees. The grid resolution used is $d_p/h = 10$. It is noted that the CPU time for these simulations is about one week on a personal computer with two CPUs.
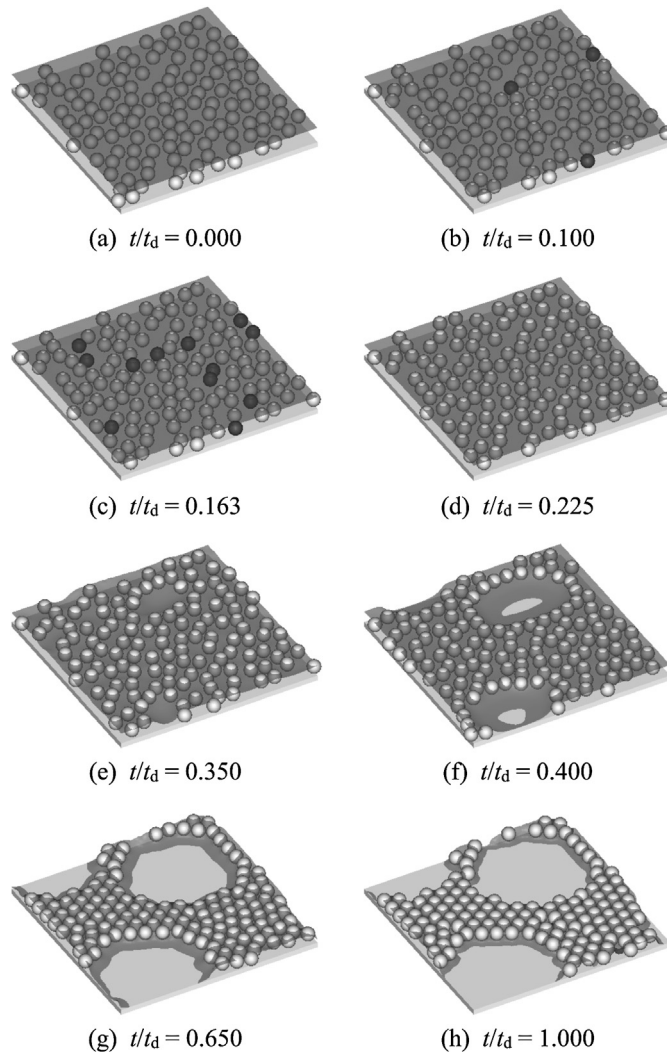
Fig. 18 shows snapshots of the hydrophilic particles and the free surface during drying. The initial height of the free surface is $1.2d_p$, in which all particles are attached on the substrate, as shown in Fig. 18(a). As the drying starts, some particles are floated from the substrate due to the Brownian motion of the particles, as shown in Fig. 18(b). Then the floating particles are in contact with the free surface, as shown in Fig. 18(c). As the free surface goes down, the floating particles are re-attached on the substrate, as shown in 18(d). From this point forward, menisci are formed around the particles. The menisci around each particle become asymmetric, because the inter-particle distances are asymmetric. As a result, net immersion capillary forces are exerted between the neighboring particles, so that the particles aggregate one another. As shown in 18(e), the aggregation of the particles produces some holes where particles do not exist. Since the holes increase the asymmetricity of menisci, the holes are enlarged with time. Then dewetting takes place on the substrate, as shown in Fig. 18(f). It can be called "particle-induced dewetting". As the holes are enlarged further, all the particles on the substrate aggregate one another, as shown in Fig. 18(g). Eventually, the volume of liquid phase approaches zero and the structure of particles are fixed on the substrate, as shown in Fig. 18(h).

Fig. 19 shows snapshots of the hydrophobic particles and the free surface during drying. The initial condition shown in Fig. 19(a) is the same as Fig. 18(a). As the drying starts, some particles are floated from the substrate due to the Brownian motion of the particles. The particles are subject to the upward vertical capillary force and protrude from the free surface, as shown in Fig. 19(b). The particles float on the free surface at the equilibrium position that depends on the contact angle. As shown in Fig. 19(c), the floating particles readily aggregate one another due to the van der Waals force, because the floating particles are free from the frictional drag from the substrate. As the aggregation proceeds, the particles at an inner region of the aggregate are re-attached on the substrate due to the van der Waals force exerted between the particles and the substrate, as shown in Fig. 19(d). This is because the particles at an inner region of the aggregate are free from the vertical capillary force. Then the number of re-attached particles increases with time, as shown in Fig. 19(e). When many particles in the aggregate are re-attached on the substrate, the free surface becomes convex upward around the aggregate. The convex free surface exerts immersion capillary forces between the aggregate and the floating particles. As a result, the remaining floating particles are attached to the aggregate, as shown in Fig. 19(f). As the free surface goes down further, dewetting takes place on the substrate, as shown in Fig. 19(g). Eventually, the volume of liquid phase approaches zero and the structure of particles are fixed on the substrate, as shown in Fig. 19(h).

The structure of particles obtained by the above simulations are quantitatively evaluated by nondimensional boundary area (NBA) proposed by the authors. The NBA represents the ratio of boundary area of aggregated particles to the summation of boundary area of each particle. A two-dimensional schematic picture of boundary area of aggregated particles is shown in Fig. 20. In the case of spherical particles with the same diameter, the boundary area can be approximated using the coordination number of each particle. Then NBA is expressed as

$$\text{NBA} = \frac{1}{\xi N}\sum_{k=0}^{\xi}\{(\xi - k)n(k)\}, \tag{90}$$

where ξ is the maximum coordination number, N is the total number of particles, $n(k)$ is the number of particles whose coordination number is k. Note that $\xi = 6$ in two dimensions and $\xi = 12$ in three dimensions. The NBA becomes 1 when all particles are completely dispersed. The NBA becomes 0 when all particles are hexagonally close packed. Namely, the NBA decreases as aggregation of the particles evolves.
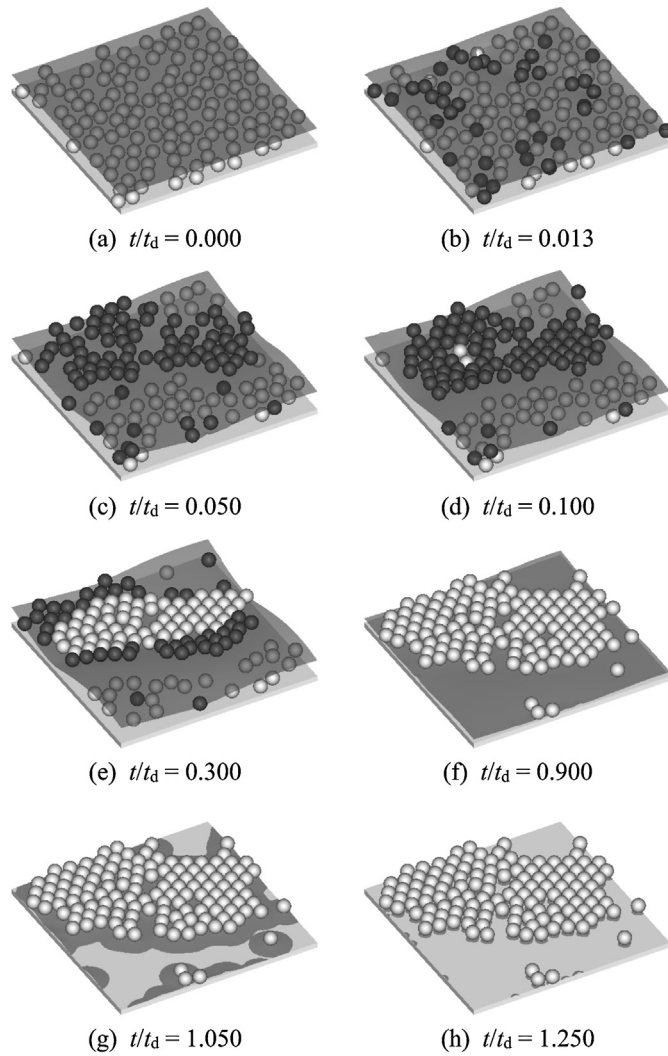
(a) $t/t_d = 0.000$ (b) $t/t_d = 0.100$

(c) $t/t_d = 0.163$ (d) $t/t_d = 0.225$

(e) $t/t_d = 0.350$ (f) $t/t_d = 0.400$

(g) $t/t_d = 0.650$ (h) $t/t_d = 1.000$

Fig. 18. Snapshots of the hydrophilic particles ($\theta = 30°$) and the free surface during drying. White particles are attached on the substrate and black particles float above the substrate. The free surface is depicted as a translucent gray surface of $\phi = 0$. The simulation time t is normalized by t_d, where $t_d = 1.2 d_p \rho_l / \dot{\omega}$ is the nominal drying time of the liquid film without particles.

Fig. 21 shows NBA as a function of dimensionless time. Since a monolayer structure of particles is investigated here, NBA in two dimensions is illustrated in the figure. For hydrophilic particles, the aggregation of the particles takes place in two steps. At the first step, a slight aggregation of the floating particles takes place from time 18(b) to time 18(d). The driving force of the aggregation at the first step is the van der Waals force. At the second step, a significant aggregation of the particles attached on the substrate takes place from time 18(e) to time 18(g). The driving force of the aggregation at the second step is the immersion capillary force. The major part of the aggregation takes place after the dewetting at time 18(f). For hydrophobic particles, on the other hand, the aggregation of the particles continuously takes place just after the drying starts. The aggregation has been almost finished until all particles are re-attached on the substrate at time 19(f). In other words, the aggregation takes place before the dewetting at time 19(g). Although the hydrophobic particles aggregate earlier than the hydrophilic particles, the hydrophilic particles aggregate more significantly than the hydrophobic particles when the drying is completed. This is because the hydrophilic particles are subject to the strong immersion capillary force in the final stage of the drying.

5. Conclusion

In this paper, we have presented a new direct simulation method for a drying colloidal suspension on a substrate. A key issue of the present method is the immersed free surface (IFS) model to estimate accurately and efficiently the capillary forces exerted on the particles, which has been developed by the authors. Using the IFS model along with the immersed boundary (IB) method and the level set (LS) method, we have accomplished a three-way coupling of the fluid flow, the free

(a) $t/t_d = 0.000$ (b) $t/t_d = 0.013$

(c) $t/t_d = 0.050$ (d) $t/t_d = 0.100$

(e) $t/t_d = 0.300$ (f) $t/t_d = 0.900$

(g) $t/t_d = 1.050$ (h) $t/t_d = 1.250$

Fig. 19. Snapshots of the hydrophobic particles ($\theta = 120°$) and the free surface during drying. White particles are attached on the substrate and black particles float above the substrate. The free surface is depicted as a translucent gray surface of $\phi = 0$. The simulation time t is normalized by t_d, where $t_d = 1.2 d_p \rho_l / \dot{\omega}$ is the nominal drying time of the liquid film without particles.
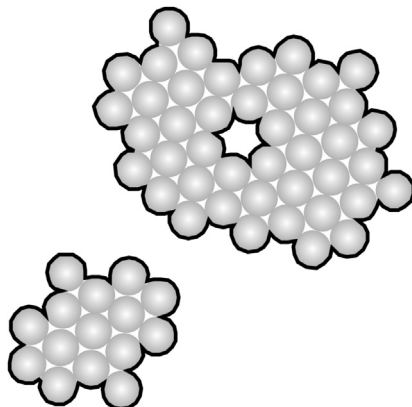
Fig. 20. A two-dimensional schematic picture of boundary area of aggregated particles that is depicted as thick black curves.
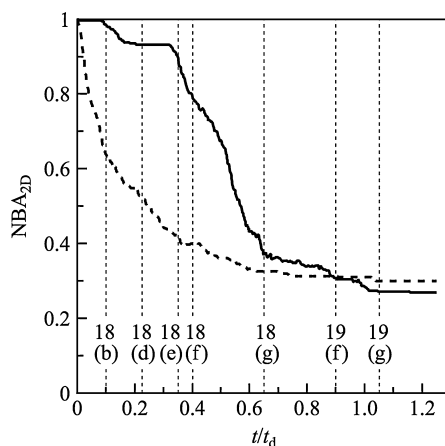
Fig. 21. NBA as a function of dimensionless time. The NBA in two dimensions for hydrophilic particles and hydrophobic particles are depicted as the solid curve and the dashed curve, respectively. The times 18(b), (d)–(g) in the figure correspond to Figs. 18(b), (d)–(g), respectively. The times 19(f) and (g) in the figure correspond to Figs. 19(f) and (g), respectively.

surface motion and the particle motion. In addition, we have developed a way of curvature estimation using virtual grid differencing to calculate the surface tension accurately.

Some simulations have been performed to demonstrate the present method. In the simulation of a still droplet, we have shown that the present way of curvature estimation is superior to the conventional way of curvature estimation in terms of accuracy. Compared to the conventional way, the present way has induced a small amount of spurious flows that may cause a critical error with simulations of free surface flow. It has been also shown that the present way of curvature estimation is insensitive to the grid resolution and has a good performance even in a coarse grid. In the simulation of a sphere moving across a free surface and the simulation of two spheres moving along a free surface, we have shown that the IFS model reproduces the deformation of menisci and the capillary force exerted on the spheres. In addition to a quantitative validation for still spheres in our previous work [38], the present study has given a quantitative validation for mobile spheres including the investigation on the grid dependency of the model. As a result, it has been shown that the estimation of the lateral capillary force exerted on two spheres requires a higher grid resolution than the estimation of the vertical capillary force exerted on a sphere. Furthermore, simulations of drying colloidal suspension containing 130 spherical particles have been performed to demonstrate the applicability of the present method to actual systems. As a result, we have shown that the mechanism of structure formation of the hydrophobic particles is much different from that of the hydrophilic particles. The hydrophilic particles have aggregated on the substrate under the influence of dewetting of the liquid film. On the other hand, the hydrophobic particles have aggregated on the substrate before dewetting. The above mechanism of the structure formation has been clarified by use of the present simulation method that has the capability of calculating the capillary force exerted on mobile particles. The capability of the present method can be helpful to clarify the formation mechanism of a variety of monolayer structures of colloidal particles during drying, such as crystal structure, amorphous structure and networked structure.

In addition to the capillary force, the present method models the stochastic hydrodynamic force, the frictional force and the van der Waals force. These forces can have an substantial influence on the microscopic structure of the particles after drying of the liquid, because these forces control the rearrangement of the particles that are in contact one another. For example, a smaller frictional force will reduce point defects in the aggregates of the particles, so that the NBA of the final structure of the particles will be decreased. Further investigations are required to clarify the influence of these forces on the structure formation of the particles during drying. A possible improvement in the present method is an introduction of the transport equations of energy and vapor to estimate a variable vaporization mass flow rate that has been a constant value in this paper. The improvement enables us to solve accurately the motion of a highly deformed free surface, because the vaporization mass flow rate at a highly deformed free surface can be different from that at a flat free surface. In the near future, we will apply our simulation method to the structure formation containing a highly deformed free surface, such as cracking and buckling of a particulate film during drying.

Acknowledgement

References

[1] X. Ye, L. Qi, Two-dimensionally patterned nanostructures based on monolayer colloidal crystals: controllable fabrication, assembly, and applications, Nano Today 6 (2011) 608–631.

[2] P.A. Kralchevsky, N.D. Denkov, Capillary forces and structuring in layers of colloid particles, Curr. Opin. Colloid Interface Sci. 6 (2001) 383–401.
[3] M. Habibi, P. Moller, A. Fall, S. Rafai, D. Bonn, Pattern formation by dewetting and evaporating sedimenting suspensions, Soft Matter 8 (2012) 4682–4686.
[4] J. Ma, G. Jing, Possible origin of the crack pattern in deposition films formed from a drying colloidal suspension, Phys. Rev. E 86 (2012) 061406.
[5] Y. Huang, J. Zhou, B. Su, L. Shi, J. Wang, S. Chen, L. Wang, J. Zi, Y. Song, L. Jiang, Colloidal photonic crystals with narrow stopbands assembled from low-adhesive superhydrophobic substrates, J. Am. Chem. Soc. 134 (2012) 17053–17058.
[6] S. Watanabe, Y. Mino, Y. Ichikawa, M.T. Miyahara, Spontaneous formation of cluster array of gold particles by convective self-assembly, Langmuir 28 (2012) 12982–12988.
[7] E. Senses, M. Black, T. Cunningham, S.A. Sukhishvili, P. Akcora, Spatial ordering of colloids in a drying aqueous polymer droplet, Langmuir 29 (2013) 2588–2594.
[8] K. Yamaguchi, S. Inasawa, Y. Yamaguchi, Optical anisotropy in packed isotropic spherical particles: indication of nanometer scale anisotropy in packing structure, Phys. Chem. Chem. Phys. 15 (2013) 2897–2902.
[9] E. Widjaja, M.T. Harris, Particle deposition study during sessile drop evaporation, AIChE J. 54 (2008) 2250–2260.
[10] R.W. Style, S.S.L. Peppin, Crust formation in drying colloidal suspensions, Proc. R. Soc. A 467 (2011) 174–193.
[11] I.V. Vodolazskaya, Yu.Yu. Tarasevich, The model of drying sessile drop of colloidal solution, Mod. Phys. Lett. B 25 (2011) 1303–1310.
[12] K. Maki, S. Kumar, Fast evaporation of spreading droplets of colloidal suspensions, Langmuir 27 (2011) 11347–11363.
[13] Ĺ. Fraštia, A.J. Archer, U. Thiele, Modeling the formation of structured deposits at receding contact lines of evaporating solutions and suspensions, Soft Matter 8 (2012) 11363–11386.
[14] A.S. Joshi, Y. Sun, Numerical simulation of colloidal drop deposition dynamics on patterned substrates for printable electronics fabrication, J. Disp. Technol. 6 (2010) 579–585.
[15] A. Sand, J. Kniivilä, M. Toivakka, T. Hjelt, Structure formation mechanisms in consolidating pigment coatings – simulation and visualisation, Chem. Eng. Process. 50 (2011) 574–582.
[16] C.S. Peskin, The immersed boundary method, Acta Numer. 11 (2002) 479–517.
[17] T. Kajishima, S. Takiguchi, Interaction between particle clusters and particle-induced turbulence, Int. J. Heat Fluid Flow 23 (2002) 639–646.
[18] Y. Nakayama, R. Yamamoto, Simulation method to resolve hydrodynamic interactions in colloidal dispersions, Phys. Rev. E 71 (2005) 036707.
[19] Z.-G. Feng, E.E. Michaelides, Proteus: a direct forcing method in the simulations of particulate flows, J. Comput. Phys. 202 (2005) 20–51.
[20] T. Kempe, J. Fröhlich, An improved immersed boundary method with direct forcing for the simulation of particle laden flows, J. Comput. Phys. 231 (2012) 3663–3684.
[21] W.-P. Breugem, A second-order accurate immersed boundary method for fully resolved simulations of particle-laden flows, J. Comput. Phys. 231 (2012) 4469–4498.
[22] L.D. Landau, E.M. Lifshitz, Fluid Mechanics, Pergamon Press, 1959.
[23] J.B. Bell, A.L. Garcia, S.A. Williams, Numerical methods for the stochastic Landau–Lifshitz Navier–Stokes equations, Phys. Rev. E 76 (2007) 016708.
[24] N. Sharma, N.A. Patankar, Direct numerical simulation of the Brownian motion of particles by using fluctuating hydrodynamic equations, J. Comput. Phys. 201 (2004) 466–486.
[25] P. Atzberger, Velocity correlations of a thermally fluctuating Brownian particle: a novel model of the hydrodynamic coupling, Phys. Lett. A 351 (2006) 225–230.
[26] M. Fujita, Y. Yamaguchi, Simulation model of concentrated colloidal nanoparticulate flows, Phys. Rev. E 77 (2008) 026706.
[27] T. Ando, K. Akamatsu, M. Fujita, S. Nakao, Direct simulation model of concentrated particulate flow in pressure-driven dead-end microfiltration, J. Chem. Eng. Jpn. 43 (2010) 815–828.
[28] Y.C. Chang, T.Y. Hou, B. Merriman, S. Osher, A level set formulation of Eulerian interface capturing methods for incompressible fluid flows, J. Comput. Phys. 124 (1996) 449–464.
[29] C.W. Hirt, B.D. Nichols, Volume of fluid (VOF) method for the dynamics of free boundaries, J. Comput. Phys. 39 (1981) 201–225.
[30] D.M. Anderson, G.B. McFadden, A.A. Wheeler, Diffuse-interface methods in fluid mechanics, Annu. Rev. Fluid Mech. 30 (1998) 139–165.
[31] T. Yabe, F. Xiao, T. Utsumi, The constrained interpolation profile method for multiphase analysis, J. Comput. Phys. 169 (2001) 556–593.
[32] G. Tomar, G. Biswas, A. Sharma, A. Agrawal, Numerical simulation of bubble growth in film boiling using a coupled level-set and volume-of-fluid method, Phys. Fluids 17 (2005) 112103.
[33] X.-Y. Luo, M.-J. Ni, A. Ying, M.A. Abdou, Numerical modeling for multiphase incompressible flow with phase change, Numer. Heat Transf., Part B, Fundam. 48 (2005) 425–444.
[34] S. Tanguy, T. Ménard, A. Berlemont, A level set method for vaporizing two-phase flows, J. Comput. Phys. 221 (2007) 837–853.
[35] F. Gibou, L. Chen, D. Nguyen, S. Banerjee, A level set based sharp interface method for the multiphase incompressible Navier–Stokes equations with phase change, J. Comput. Phys. 222 (2007) 536–555.
[36] G. Son, A level-set method for analysis of microdroplet evaporation on a heated surface, J. Mech. Sci. Technol. 24 (2010) 991–997.
[37] D.Z. Guo, D.L. Sun, Z.Y. Li, W.Q. Tao, Phase change heat transfer simulation for boiling bubbles arising from a vapor film by the VOSET method, Numer. Heat Transf., Part A, Appl. 59 (2011) 857–881.
[38] M. Fujita, O. Koike, Y. Yamaguchi, Computation of capillary interactions among many particles at free surface, Appl. Phys. Express 6 (2013) 036501.
[39] G. Son, V.K. Dhir, A level set method for analysis of film boiling on an immersed solid surface, Numer. Heat Transf., Part B, Fundam. 52 (2007) 153–177.
[40] J. Schlottke, B. Weigand, Direct numerical simulation of evaporating droplets, J. Comput. Phys. 227 (2008) 5215–5237.
[41] J.U. Brackbill, D.B. Kothe, C. Zemach, A continuum method for modeling surface tension, J. Comput. Phys. 100 (1992) 335–354.
[42] J.B. Bell, A.L. Garcia, S.A. Williams, Computational fluctuating fluid dynamics, Modél. Math. Anal. Numér. 44 (2010) 1085–1105.
[43] S. Osher, R. Fedkiw, Level Set Methods and Dynamic Implicit Surfaces, Springer, 2003.
[44] M. Uhlmann, An immersed boundary method with direct forcing for the simulation of particulate flows, J. Comput. Phys. 209 (2005) 448–476.
[45] P.A. Cundall, O.D.L. Strack, A discrete numerical model for granular assemblies, Geotechnique 29 (1979) 47–65.
[46] Y. Tsuji, T. Tanaka, T. Ishida, Lagrangian numerical simulation of plug flow of cohesionless particles in a horizontal pipe, Powder Technol. 71 (1992) 239–250.
[47] H. Nishikawa, M. Fujita, S. Maenosono, Y. Yamaguchi, T. Okubo, Effect of frictional force on the formation of colloidal particle monolayer during drying – study using discrete element method, KONA Powder Part. J. 24 (2006) 192–202.
[48] M. Fujita, Y. Yamaguchi, Multiscale simulation method for self-organization of nanoparticles in dense suspension, J. Comput. Phys. 223 (2007) 108–120.
[49] M. Fujita, Y. Yamaguchi, Development of three-dimensional structure formation simulator of colloidal nanoparticles during drying, J. Chem. Eng. Jpn. 39 (2006) 83–89.
[50] J.N. Israelachvili, Intermolecular and Surface Forces, Academic Press, 1992.
[51] C.-W. Shu, S. Osher, Efficient implementation of essentially non-oscillatory shock-capturing schemes, J. Comput. Phys. 77 (1988) 439–471.
[52] G.-S. Jiang, D. Peng, Weighted ENO schemes for Hamilton–Jacobi equations, SIAM J. Sci. Comput. 21 (2000) 2126–2143.
[53] S.J. Cummins, M.M. Francois, D.B. Kothe, Estimating curvature from volume fractions, J. Comput. Phys. 83 (2005) 425–434.
[54] M.M. Francois, S.J. Cummins, E.D. Dendy, D.B. Kothe, J.M. Sicilian, M.W. Williams, A balanced-force algorithm for continuous and sharp interfacial surface tension models within a volume tracking framework, J. Comput. Phys. 213 (2006) 141–173.

[55] S. Popinet, An accurate adaptive solver for surface-tension-driven interfacial flows, J. Comput. Phys. 228 (2009) 5838–5866.
[56] M. Sussman, M. Ohta, A stable and efficient method for treating surface tension in incompressible two-phase flow, SIAM J. Sci. Comput. 31 (2009) 2447–2471.
[57] K. Yokoi, A practical numerical framework for free surface flows based on CLSVOF method, multi-moment methods and density-scaled CSF model: numerical simulations of droplet splashing, J. Comput. Phys. 232 (2013) 252–271.
[58] A.A. Amsden, F.H. Harlow, The SMAC method: a numerical technique for calculating incompressible fluid flows, Los Alamos Scientific Laboratory Rep. LA-4370, 1970.
[59] C.A.J. Fletcher, Computational Techniques for Fluid Dynamics I – Fundamental and General Techniques, 2nd ed., Springer, 1991.
[60] M. Kang, R.P. Fedkiw, X.-D. Liu, A boundary condition capturing method for multiphase incompressible flow, J. Sci. Comput. 15 (2000) 323–360.
[61] L. Rayleigh, On the capillary phenomena of jets, Proc. Phys. Soc. Lond. 29 (1879) 71–97.